Functional fluorescently-tagged human profilin

Morgan L. Pimm[1], Xinbei Liu[1], Farzana Tuli[1], Ashley Lojko[1], and Jessica L. Henty-Ridilla ✉[1,2]

[1]Department of Biochemistry and Molecular Biology, SUNY Upstate Medical University, Syracuse, NY, 13210, USA.
[2]Department of Neuroscience and Physiology, SUNY Upstate Medical University, Syracuse, NY, 13210, USA.

Profilin is an essential regulator of actin and microtubule dynamics and therefore a critical control point for the normal division, motility, and morphology of cells. Most studies of profilin have focused on biochemical investigations using purified protein because high cellular concentrations (121 µM) present challenges for conventional imaging modalities. In addition, past studies that employed direct labeling or conventional fusion protein strategies compromised different facets of profilin function. We engineered a fluorescently-labeled profilin that retains native activities with respect to phosphoinositide lipids, actin monomers, formin-mediated actin assembly, and microtubule polymerization. This fluorescent profilin directly binds to dimers of tubulin (k_D = 1.7 µM) and the microtubule lattice (k_D = 10 µM) to stimulate microtubule assembly. In cells, our tagged profilin fully rescues profilin-1$^{(-/-)}$ cells from knockout-induced perturbations to cell shape, actin filament architecture, and microtubule arrays. Thus, this labeled profilin-1 is a reliable tool to investigate the dynamic interactions of profilin with actin or microtubules in live cell and in vitro applications.

profilin | actin | microtubules | tubulin | formin | PIP-lipids
Correspondence: ***ridillaj@upstate.edu***

Introduction

Profilin is a small (~15 kDa) cytosolic protein with binding regions required for interacting with phosphoinositide (PIP) lipids, actin monomers, poly-L-proline (PLP) containing ligands, and microtubules. Through these interactions, it plays critical roles in signal transduction cascades, apoptosis, motility, phagocytosis, and mitosis (Davey and Moens, 2020; Pimm et al., 2020; Karlsson and Dráber, 2021). Profilin is a classic regulator of actin dynamics that directly binds actin monomers to suppress actin filament assembly. Interactions between profilin and PIP lipids further fine tune actin assembly in cell signaling cascades (Lassing and Lindberg, 1985; Krishnan and Moens, 2009; Ding et al., 2012; Davey and Moens, 2020). In contrast to these mechanisms, profilin stimulates actin polymerization through interactions mediated by poly-L-proline (PLP) tracts in key regulators like formins or Ena/VASP. Combined, these activities effectively regulate many properties of the actin monomer pool and bias actin polymerization in favor of straight filament architectures (Henty-Ridilla and Goode, 2015; Rotty et al., 2015; Suarez et al., 2015; Suarez and Kovar, 2016; Skruber et al., 2018). Despite similar concentrations, not all cellular profilin is bound to actin monomers (Goldschmidt-Clermont et al., 1992; Kaiser et al., 1999; Skruber et al., 2018, 2020; Zweifel and Courtemanche, 2020). Some profilin outcompetes actin bound to intracellular lipids present on membranes and vesicles to transmit distinct cellular signals (Lassing and Lindberg, 1985; Davey and Moens, 2020). Profilin also directly regulates cellular microtubule dynamics and organization (Witke et al., 1998; Nejedla et al., 2016; Henty-Ridilla et al., 2017; Pinto-Costa and Sousa, 2019; Pimm et al., 2020; Karlsson and Dráber, 2021; Nejedlá et al., 2021; Pimm and Henty-Ridilla, 2021). Despite the importance in regulating these essential activities, existing profilin probes compromise different facets of function. Consequently, most of what is known about profilin has been ascertained outside of the cell, determined from in vitro biochemical assays.

Conventional protein tagging strategies compromise profilin functions (Skruber et al., 2018; Pimm et al., 2020). To complicate matters further, because profilin is present at high cellular concentrations (8-100 µM, depending on the cell type), fluorescent probes often oversaturate signals collected from conventional imaging modalities (Wittenmayer et al., 2000; Henty-Ridilla et al., 2017; Nejedla et al., 2017; Funk et al., 2019; Nejedlá et al., 2021). Direct (cysteine/maleimide) labeling approaches for detecting individual molecules of protein require 4-5 amino acid modifications in profilin. Each of these substitutions results in aggregation and compromised function in human profilin (Vidali and Hepler, 1997; Vinson et al., 1998; Kaiser et al., 1999; Henty-Ridilla et al., 2017). Microinjection experiments require advanced imaging tools, skills, and directly labeled profilin, but can be performed in live-cells without overexpression. While this technique is challenging to perform, it is able to localize profilin to sites of actin assembly, lipid membranes, and the nucleus (Lassing and Lindberg, 1985; Hartwig et al., 1989; Tarachandani and Wang, 1996; Kaiser et al., 1999). Positioning a GFP-derived fluorescent tag on the C- or N-terminus disrupts PLP- and PIP-binding interactions, effectively rendering the fluorescent version flawed for critical measurements in cells (Wittenmayer et al., 2000; Antoine et al., 2020). Splitting profilin by inserting a fluorescent tag in a protruding loop in the center of the protein retains normal binding affinity for PLP and lipids, but compromises actin functions (Nejedla et al., 2017; Karlsson and Dráber, 2021; Nejedlá et al., 2021). This approach cannot be applied to all profilins equally.

A popular imaging approach to circumvent some of these issues employs anti-profilin antibodies to stain detergent-extracted remnants of fixed cells (Henty-Ridilla et al., 2017; Nejedla et al., 2017; DeCaprio and Kohl, 2020; Nejedlá et al., 2021). This technique unambiguously localizes profilin to stable cytoskeletal structures (i.e., stress fibers, the sides of microtubules, nuclear components) in cells. However, this technique obscures the fine spatiotemporal details required to measure the flux or dynamics of cellular pools of profilin. To

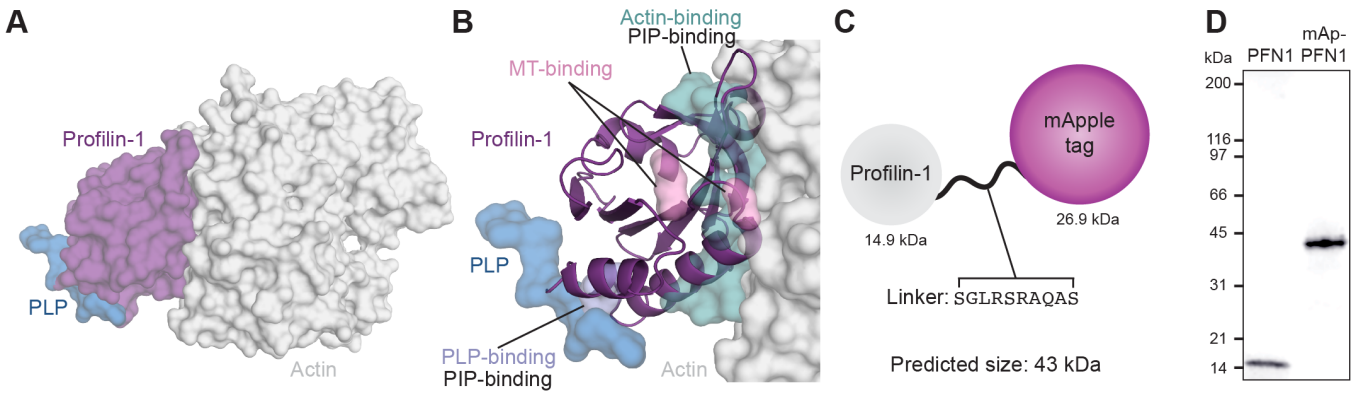

Fig. 1. Strategy for fluorescently-tagging and purifying profilin-1. (A) View of profilin (purple) interacting with actin (gray) and the poly-L-proline (PLP) region of VASP (blue), modeled using PDB: 2BTF (Schutt et al., 1993) and PDB: 2PAV (Ferron et al., 2007). **(B)** Magnified view showing profilin surfaces in contact with actin and PLP. The positions of key residues are highlighted as follows: actin-binding residues (teal), PLP-binding (Y6D; light blue), and microtubule binding (M114, G118; pink). **(C)** Design of tagged-PFN1 fusion protein. The tag (mApple or Halo) was positioned at the N-terminus of Human profilin-1 following a ten amino acid linker sequence (SGLRSRAQAS). **(D)** Coomassie-stained SDS-PAGE gel of profilin (PFN1) and mApple-profilin-1 (mAp-PFN1) expressed and purified from bacterial lysates.

date >10 different engineered profilins have been produced, yet no uniform tagging strategy is able to retain native profilin functions or can be applied across species, isoforms, or varying cellular situations. We engineered and characterized a new fluorescent profilin. We overcome many of the drawbacks of previous approaches using a flexible linker at the N-terminus coupled with GFP-derived or titratable self-labeling approaches (i.e., SNAP-, Halo-, or CLIP-tags). Our new fluorescently-tagged profilin behaves like the native version for binding PIP lipids, actin monomers, PLP-containing ligands, and microtubules. In cells, tagged profilin fully rescues knockout-induced perturbations to cell shape, actin filament architecture, and microtubule arrays. We anticipate these tools may be used to decipher the role of profilin in diverse cells and situations.

Results

Design of tagged profilin.

Tagging human profilin without compromising its canonical activities has been extremely challenging. Profilin is considerably smaller than the smallest fluorescent tags (profilin is 15 kDa whereas GFP is 27 kDa). Traditional direct labeling approaches are cytotoxic and disrupt actin-based functions (Henty-Ridilla et al., 2017; Skruber et al., 2018; Pimm et al., 2020). Critical aspects of profilin's function occur through conserved binding sites for PIP lipids, actin monomers, poly-L-proline motifs, or microtubules (Figures 1A and 1B). Estimates of cellular profilin concentration are very high depending on the cell type (Koestler et al., 2009; Funk et al., 2019), presenting challenges to localizing fluorescent probes or antibodies. To directly monitor profilin activities, we engineered two versions of human profilin-1 visible either with an mApple fluorescent probe or as Halo-tagged single molecules (Figure 1C). We cloned mApple- or Halo-tags fused to a ten amino acid flexible linker on the N-terminus of human profilin-1. We expressed and purified recombinant versions of wild-type and mApple-tagged profilin to compare the effects of tagged profilin in several in vitro biochemistry assays. SDS-PAGE analysis revealed that the wild-type and tagged versions of profilin were the expected size and highly pure (Figure 1D).

mApple-profilin binds phosphoinositide lipids with similar affinity as untagged profilin.

All profilins are known to bind some form of phosphoinositide (PIP) lipid alone or in complex with actin monomers. Association between PIP lipids and profilin occurs on two different binding surfaces on profilin, overlapping with either the actin- or PLP-binding residues (Figure 1B) (Hartwig et al., 1989; Goldschmidt-Clermont et al., 1990; Lambrechts et al., 2002; Skare and Karlsson, 2002; Ferron et al., 2007; Nejedla et al., 2017). While there are many versions of PIP signaling lipids, PI(4,5)P_2 is the best-characterized regulator of actin organization (Davey and Moens, 2020). At the plasma membrane PI(4,5)P_2 directly interacts with profilin to inhibit actin dynamics and regulate overall cell morphology (Niggli, 2005). Profilin also binds PI(3,5)P_2 which regulates critical signal transduction events through intracellular vesicles to the early endosome (Goldschmidt-Clermont et al., 1990; Martys et al., 1996; Dong et al., 2000). We performed liposome pelleting assays for PI(3,5)P_2 or PI(4,5)P_2 (Figure 2A) (Banerjee and Kane, 2017; Chandra et al., 2019). We detected mApple-profilin bound to either PI(3,5)P_2 or PI(4,5)P_2 containing liposomes via western blots using profilin-specific antibodies. Untagged profilin did not pellet in buffer controls lacking liposomes. However, antibodies detected profilin-1 in the liposome pellet of reactions containing control lipids or either PI(3,5)P_2 or PI(4,5)P_2 lipids (Figures 2B and 2D). Similar to wild-type, mApple-profilin was only detected in reactions containing PIP lipids (Figures 2C and 2D). Quantitative comparisons subtracting the amount of profilin-bound non-specifically to liposome controls, demonstrate that mApple-profilin binds either PI(3,5)P_2 or PI(4,5)P_2 with similar affinity to untagged profilin. (Figures 2D and 2E). Thus, mApple-tagged profilin retains functional interactions with two important PIP lipids.

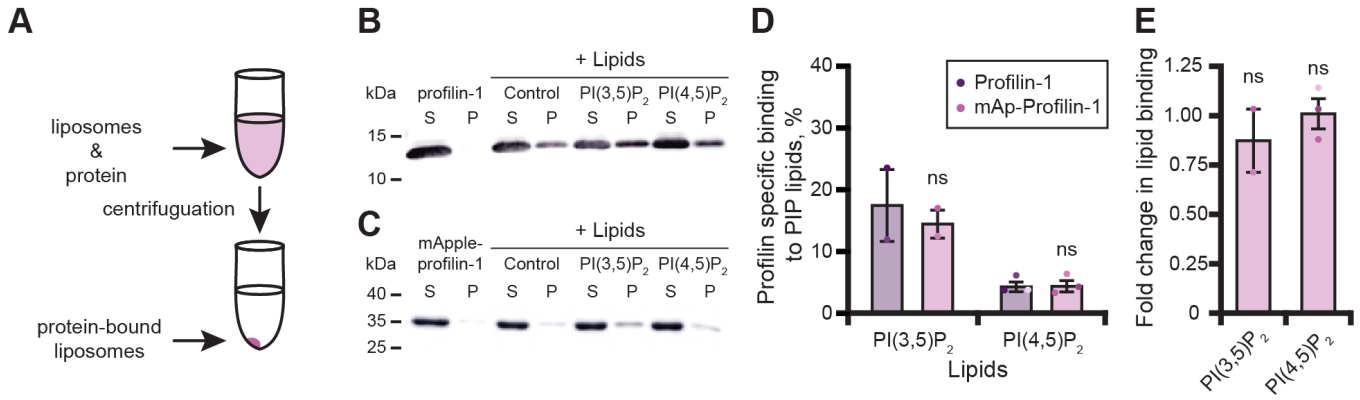

Fig. 2. Tagged profilin binds phosphoinositide (PIP)-lipids. (A) Schematic detailing liposome pelleting assays used to determine the binding efficiency of profilin proteins for phosphatidylinositol 3,5-bisphoshate ($PI(3,5)P_2$) or phosphatidylinositol 4,5-bisphoshate ($PI(4,5)P_2$) lipids. **(B)** Representative western blot of supernatants and pellets from liposome pelleting assays containing 1 µM profilin in absence (control) or presence of 0.33 mM of either PIP-lipid. Profilin-1 B 10 was used as a primary antibody (1:5,000 dilution; SantaCruz 137235) and goat anti-mouse 926-32210 was used as the secondary antibody (1:10,000 dilution; LiCor Biosciences). **(C)** Representative western blot of supernatants and pellets from liposome pelleting assays as in (B) for mApple-profilin. **(D)** Band intensities from western blots in (B and C) were quantified to determine the amount of profilin-specific binding to $PI(3,5)P_2$ or $PI(4,5)P_2$. **(E)** The fold change in lipid binding of mApple-profilin compared to the untagged version. The affinity of tagged profilin for either lipid was not significantly different from the untagged version. Shaded values in (D) and (E) represent the individual data points used to determine the mean from (n = 2-3) independent experiments. Error bars indicate standard error. Significant differences were determined by Student's t-test. ns, not significantly different from control. Images of full blots are present in Figure S1.

Direct visualization of fluorescent-profilin with polymerizing actin filaments.

Profilin binds to actin monomers as a 1:1 complex that strongly suppresses actin nucleation or minus-end monomer addition through steric hinderance interactions (Blanchoin et al., 2014). However, profilin binding interactions are typically indirectly assessed, recorded as reduced total actin polymerization in bulk assays, or reduced actin filament nucleation rates in microscopy-based assays that monitor actin polymerization. To date, the most reliable approach for measuring direct binding between profilin and actin monomers is isothermal titration calorimetry (ITC) (K_D = 0.1 µM; Wen et al., 2008). However, the major limitation to this approach is the requirement of copious amounts of protein for measurements. We used fluorescence anisotropy to measure the binding affinity between profilin and Oregon-Green (OG)-labeled monomeric actin (Figure S2). We were unable to detect a change in anisotropy at any concentration of profilin used, consistent with previous reports (Vinson et al., 1998; Kaiser et al., 1999). Several studies demonstrate that thymosin β4 (Tβ4) competes with profilin to bind actin monomers (Goldschmidt-Clermont et al., 1992; Aguda et al., 2006; Xue et al., 2014). First, we confirmed the binding affinity of GFP-Tβ4 for unlabeled actin monomers using fluorescence anisotropy (k_D = 5.4 ± 6.7 nM) (Figure 3A). We next performed competitive fluorescence anisotropy assays in the presence of GFP-Tβ4 to determine the affinity of actin monomers for either profilin protein (wild-type or mApple-tagged) (Figure 3B). Wild-type (k_D = 99.3 ± 12.4 nM) and fluorescently-tagged profilin (k_D = 96.3 ± 23.4 nM) bound actin monomers with affinities that were not statistically different (Figure 3B). We also confirmed the affinity of mApple-profilin and unlabeled actin monomers in the absence of GFP-Tβ4 (i.e., non-competitive assay). Fluorescent profilin directly bound actin monomers with a similar affinity (k_D = 105.2 ± 26.9 nM) (Figure 3C). Thus, this tagged profilin binds actin monomers with wild-type affinity.

We next compared the rates of actin assembly in the presence of wild-type or mApple-profilin in bulk actin-fluorescence assays (Figure 3D). Compared to the actin alone control, less total actin polymer was made in the presence of unlabeled profilin (Figure 3D). Actin filaments in the presence of mApple-profilin polymerized to similar levels as with unlabeled profilin, and less efficiently than the actin alone control. This demonstrates that both versions of profilin inhibit the spontaneous nucleation of actin filaments. To investigate this further, we used single-molecule total internal reflection fluorescence (TIRF) microscopy to directly visualize actin assembly in the presence of our various versions of profilin (Figure 3E). TIRF reactions containing wild-type profilin or mApple-profilin had similar levels of OG-actin fluorescence and less total fluorescence than actin alone controls (Figure 3E). To better understand the effects of mApple-profilin on actin assembly, we examined the nucleation and elongation phases of actin filament formation. We measured an average of 45.3 ± 1.4 filaments per field of view (FOV) in control assays where actin filaments were assembled alone (Figure 3F). We measured significantly fewer actin filaments in reactions supplemented with either untagged (21.5 ± 3.4) or mApple-profilin (19.8 ± 2.9) compared to actin alone controls (Figure 3F). The mean rate of actin filament polymerization in the presence of mApple-profilin was 10.05 ± 0.16 subunits s^{-1} μM^{-1} and is not significantly different than the untagged version measured as 10.07 ± 0.16 subunits s^{-1} μM^{-1} (Figure 3G). Neither of these rates differs significantly from the rate of free barbed-end growth obtained from reactions containing actin alone (10.07 ± 0.16 subunits s^{-1} μM^{-1}). In sum, mApple-profilin binds actin monomers, inhibits actin filament assembly, and does not alter the rate of actin filament elongation. Each of these activities is indistinguishable

from untagged profilin.

Profilin has strikingly different affinities for actin monomers (k_D = 100 nM) and for the growing ends of actin filaments (k_D = 225 μM) (Courtemanche and Pollard, 2013; Pernier et al., 2016; Funk et al., 2019; Pimm et al., 2020; Zweifel and Courtemanche, 2020). This property permits the effective disassociation of profilin from the ends of growing actin filament during polymerization (Courtemanche and Pollard, 2013; Pernier et al., 2016; Zweifel and Courtemanche, 2020). Many of the actin-assembly roles of profilin revolve around its ability to bind actin monomers. However at high stochiometric concentrations, profilin binds actin filaments and may interfere with actin elongation (Jégou et al., 2011; Courtemanche and Pollard, 2013; Funk et al., 2019; Zweifel and Courtemanche, 2020). We performed two-color TIRF microscopy to visualize the localization of mApple-profilin with polymerizing actin filaments (Figure S3A). The majority of polymerizing actin filaments visualized did not appear to have mApple-profilin associated on growing filament ends or sides (Figure S3A). One actin filament appeared to have a single-molecule of mApple-profilin associated with the growing end (Figure S3B). This single event was extremely transient and lasted for <5 s (Figures S3B and S3C). Further associations may occur on timescales and resolutions not able to be resolved with our imaging system or at concentrations closer to the predicted constant required for barbed-end association (K_D > 20 μM) (Jégou et al., 2011; Courtemanche and Pollard, 2013; Pernier et al., 2016; Funk et al., 2019; Skruber et al., 2020). Higher concentrations of fluorescent profilin may also conceal the dynamics of individual profilin molecules due to higher background fluorescence levels. These data suggest that most of mApple-profilin in these assays is associated with the actin monomer pool rather than localized to actin filaments.

Fluorescent profilin stimulates formin-based actin filament assembly.

In addition to its role as a strong inhibitor of actin filament assembly (Figure 3), profilin can simultaneously bind actin monomers and proline-rich motifs (i.e., PLP) present in cytoskeletal regulatory proteins that include: formins, Ena/VASP, and WASP/VCA-domain containing proteins that activate the Arp2/3 Complex (Reinhard et al., 1995; Gertler et al., 1996; Chang et al., 1997; Evangelista, 1997; Mammoto et al., 1998; Miki et al., 1998; Suetsugu et al., 1998; Higgs and Pollard, 1999; Evangelista et al., 2002; Rodal et al., 2003; Ferron et al., 2007). The competition for profilin-actin between different actin nucleation systems has led to the popular idea that profilin tunes specific forms of actin assembly (branched or straight filaments) depending on the concentration of active nucleation proteins present (Rotty et al., 2015; Suarez et al., 2015; Skruber et al., 2018, 2020). Therefore, we tested whether mApple-profilin was capable of actin filament assembly through the PLP-motif containing formin mDia1. Actin filaments assembled to similar levels in bulk pyrene fluorescence assays containing actin monomers and either profilin or mApple-profilin, (Figure 4A). The addition of a constitutively active formin, mDia1(FH1-C), to these reactions resulted in strongly enhanced actin polymerization compared to reactions lacking profilin (Figure 4A). Thus, mApple-profilin stimulates formin-based actin assembly indistinguishable from native profilin-1.

To investigate this hypothesis further, we used TIRF microscopy to directly visualize actin assembly in the presence of mDia1(FH1-C) and either profilin protein (Figures 4B and S4A). TIRF reactions of untagged profilin or mApple-profilin had significantly more OG-actin fluorescence compared to reactions without formin (Figure 4C). As a readout of actin filament nucleation, we counted the number of actin filaments from TIRF movies in the presence of formin (Figure 4D). Similar to experiments in assessing only profilin-actin interactions (Figure 3F), we counted significantly fewer actin filaments in reactions containing actin and either profilin (Figure 4D). We counted an average of 659.3 ± 98.3 filaments from TIRF reactions containing actin and mDia1(FH1-C), which was significantly higher ($p = 0.014$, ANOVA) than reactions containing actin alone or either actin-profilin or actin-mApple-profilin controls. Reactions containing formin and either untagged (42.7 ± 9.8 filaments) or mApple-profilin (48.3 ± 14.5 filaments) had statistically fewer filaments than control reactions assessing the combination of formin and actin ($p = 0.0004$, ANOVA), consistent with previous reports that profilin also suppresses formin nucleation (Kovar et al., 2006; Zweifel and Courtemanche, 2020). Thus, fluorescent profilin stimulates formin-mediated actin filament nucleation similar to the untagged version.

We next explored whether mApple-profilin was capable of accelerating the rate of formin-mediated actin filament elongation in TIRF microscopy assays (Figure 4E). In these reactions we measured actin filaments elongating at two different speeds. The slowest speed corresponded to the rate of actin assembly with a free barbed end (10 subunits s^{-1} μM^{-1}) (Kovar et al., 2006; Henty-Ridilla et al., 2016). The faster speed corresponded to the previously recorded rate of mDia1(FH1-C)-mediated actin filament assembly (50 subunits s^{-1}1 μM^{-1}) (Kovar et al., 2006; Henty-Ridilla et al., 2016). The accelerated rate of actin filament assembly was exclusively observed in reactions that contained actin, mDia1(FH1-C), and untagged profilin (42.7 ± 9.8 subunits s^{-1} μM^{-1}) or mApple-profilin (48.3 ± 14.5 subunits s^{-1} μM^{-1}). We also used two-color TIRF assays to investigate the localization of mApple-profilin on actin filaments in the presence of formin. We did not notice a strong association of mApple-profilin with actin filaments containing formin (Figure S4B). However, the acquisition time used for these experiments (5 s intervals) does not exclude this possibility. Thus, these results demonstrate that both version of profilin (untagged or mApple-profilin) stimulate the nucleation and elongation phases of formin-based actin assembly at comparable levels.

Profilin directly binds tubulin dimers and enhances the growth rate of microtubules in vitro.

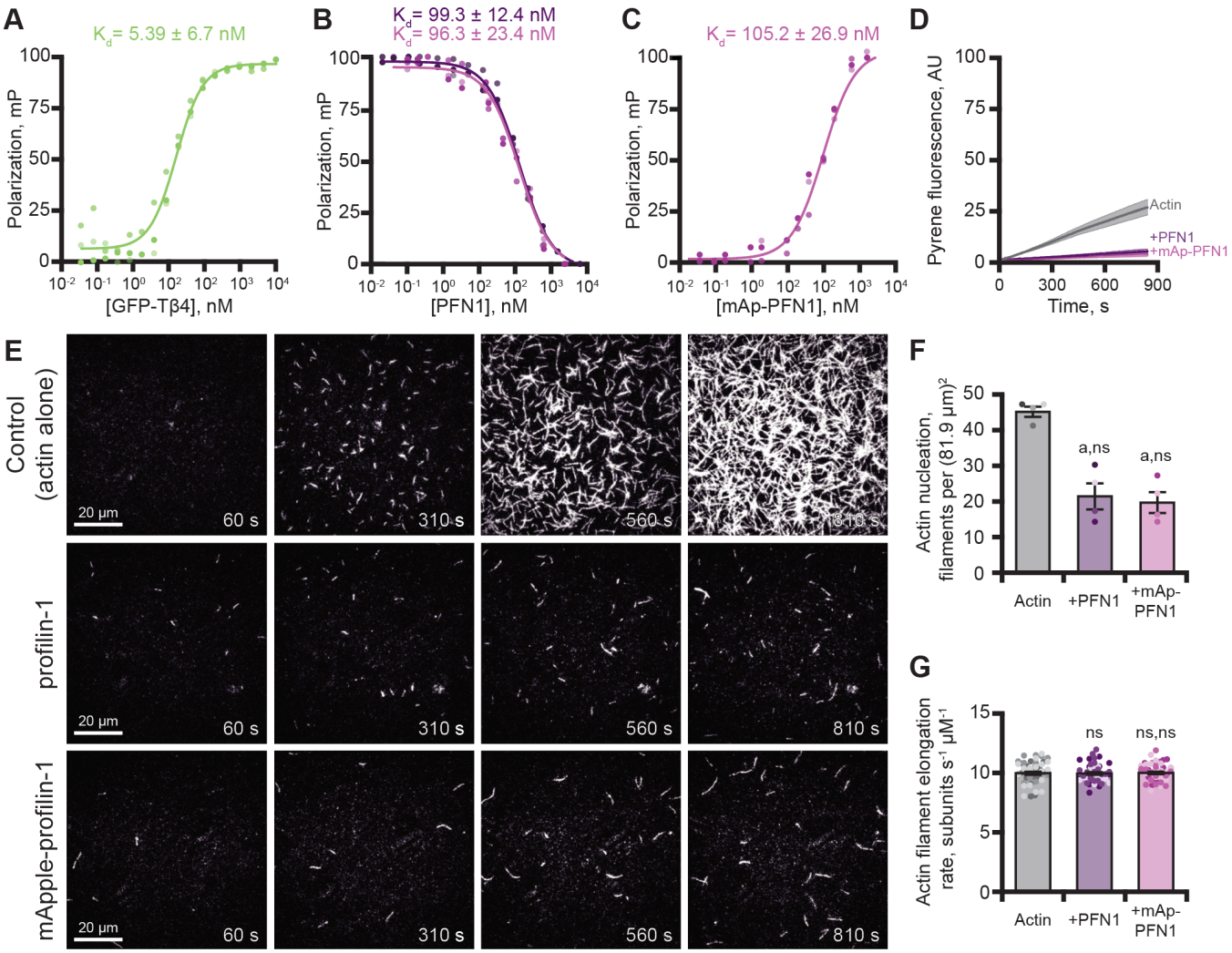

Fig. 3. Tagged profilin binds actin monomers with affinity equivalent to native profilin. (A) Fluorescence anisotropy of 10 nM GFP-thymosin β4 (GFP-Tβ4) mixed with increasing concentrations of unlabeled actin. **(B)** Competitive fluorescence anisotropy measurement of 10 nM GFP-thymosin β4, 10 nM unlabeled actin monomers, and increasing concentrations of profilin (purple) or mApple-profilin (pink). **(C)** Fluorescence anisotropy measurement of 10 nM unlabeled actin and increasing concentrations of mApple-profilin. **(D)** Bulk fluorescence comparing the rate of actin assembly with either profilin protein. Reactions contain: 2 µM actin (5% pyrene-labeled), and 3 µM profilin (PFN1) or 3 µM mApple-profilin (mAp-PFN1). Shaded values represent SEM from three independent trials. **(E)** Time lapse images from TIRF microscopy assays monitoring the assembly of 1 µM actin (20% Oregon Green (OG)-labeled, 0.6 nM biotin-actin) in the presence or absence of 3 µM profilin or 3 µM mApple-profilin. Scale bar, 20 µm. See Supplemental Movies 1 and 2. **(F)** Average number of filaments visible after 100 s of actin assembly, visualized as in (E). Data were quantified from four separate reactions (FOV) each. **(G)** Distribution of actin filament elongation rates from TIRF reactions as in (E) (n = 51 filaments per condition). Shaded values in (A-C) and (F-G) represent the individual data points used to determine the mean from (n = 4) independent experiments. Error bars indicate SE. Significant differences by one-way ANOVA with Bartlett's correction for variance: ns, not significantly different from 1 µM actin alone control; a, compared with control ($p < 0.05$).

In addition to its well-established roles regulating actin polymerization, profilin influences microtubule polymerization through direct and indirect mechanisms. We used TIRF microscopy to compare microtubule dynamics in the presence and absence of untagged profilin or mApple-profilin (Figure 5A). In all reactions, microtubules displayed instances of dynamic instability, stochastically switching between periods of growth and shortening. Microtubules in reactions containing free tubulin dimers and profilin grew at a rate 6-fold faster than tubulin alone controls, from 1.9 ± 0.2 µm $^{-1}$ min $^{-1}$ to 12.7 ± 0.3 µm $^{-1}$ min $^{-1}$ (Figures 5B and 5C) (Henty-Ridilla et al., 2017). Microtubules in experiments including mApple-profilin elongated at significantly accelerated rates (12.6 ± 0.4 µm $^{-1}$ min $^{-1}$) compared to controls ($p < 0.0001$, ANOVA). Consistent with an accelerated microtubule growth rate, the mean length of microtubules in reactions containing either profilin protein was significantly longer (Figure 5D; $p < 0.0001$, ANOVA). Microtubules polymerized in the presence of mApple or untagged profilin were also more stable (Figure 5E). Specifically, the microtubule stability index (ratio of rescue to catastrophe events) was increased in favor of more steadily growing microtubules ($p < 0.0001$, ANOVA).

Previous observations suggest that profilin increases the on rate of tubulin at microtubule ends to facilitate microtubule elongation (Henty-Ridilla et al., 2017). Consistent with this hypothesis, microtubules were observed in TIRF reactions performed at concentrations of free tubulin below the critical concentration required for microtubule assembly (Henty-Ridilla et al., 2017). While our experiments were performed above the critical concentration for microtubule assembly, we

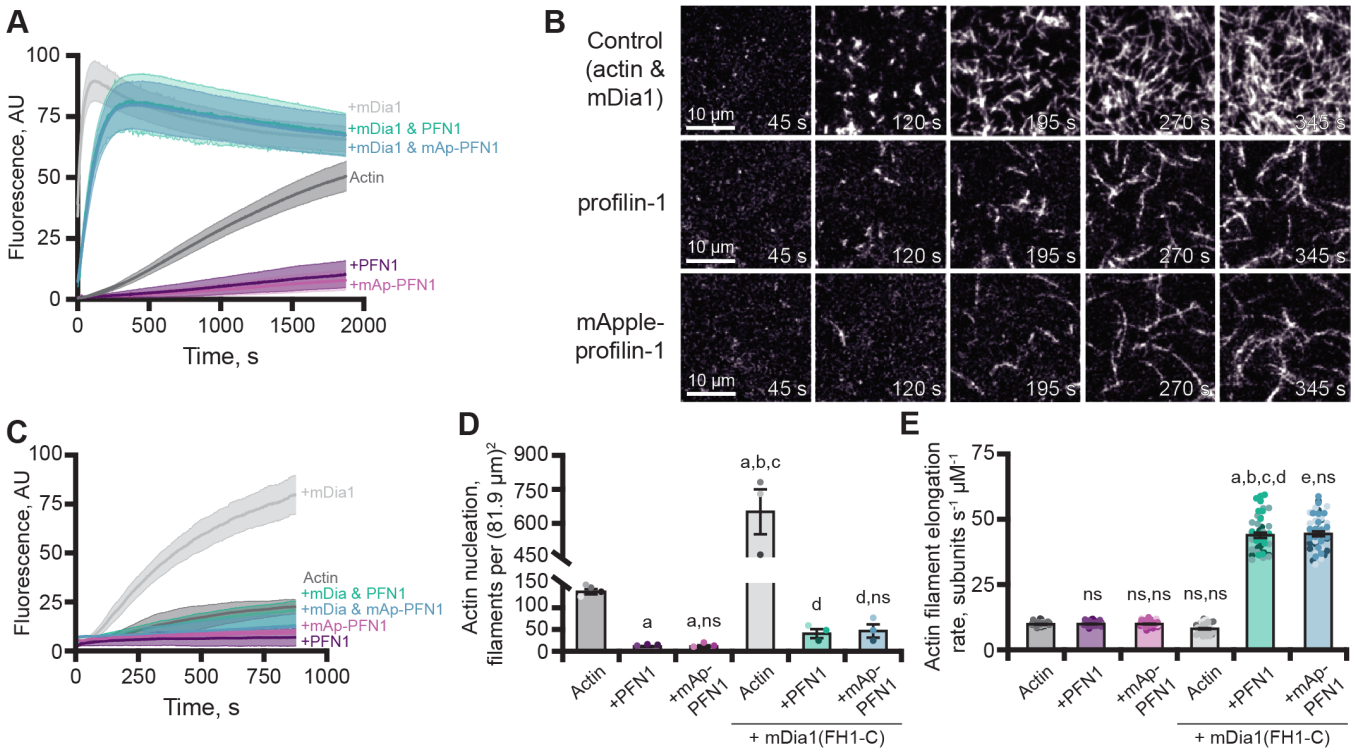

Fig. 4. Effects of tagged profilin on formin-mediated actin assembly. (A) Bulk pyrene fluorescence comparing the rate of formin-mediated actin assembly in the presence or absence of different profilins. Reactions contain: 2 µM actin (5% pyrene-labeled), 25 nM mDia1 (FH1-C), and 5 µM profilin (PFN1) or 5 µM mApple-profilin (mAp-PFN1). Shaded values represent SEM from three independent trials. **(B)** Representative images from time lapse TIRF experiments. Reactions contain: 1 µM actin (10% Alexa-647-labeled, 0.6 nM biotin-actin), 25 nM mDia1 (FH1-C), and 5 µM profilin (PFN1) or 5 µM mApple-profilin (mAp-PFN1). Scale bar, 10 µm. See Supplemental Movies 3 and 4. **(C)** Graph of total actin polymer mass over time, averaged from the fluorescence intensity of multiple fields of view (FOV) from TIRF reactions. Shading indicates SE for each condition. **(D)** Average number of filaments visible after 100 s of actin assembly, visualized as in (B). **(E)** Actin filament elongation rates from TIRF reactions as in (B) (n = 51 filaments per condition). Shaded values in (D-E) represent the individual data points used to determine the mean from at least three independent experiments. Error bars indicate SE. Significant differences by one-way ANOVA with Bartlett's correction for variance: ns, not significantly different from the actin alone control; a, compared with control ($p < 0.05$); b, compared with untagged profilin ($p < 0.05$); c, compared with mApple-profilin (mAp-PFN1) ($p<0.05$); d, compared with actin and mDia1(FH1-C) control ($p<0.05$); e, significantly different from all conditions except actin, mDia1(FH1-C) and untagged profilin ($p<0.05$).

observed a comparable and significant increase in the mean number of microtubules present in FOVs from TIRF assays performed in the presence of either profilin protein (Figure 5F) ($p = 0.0048$, ANOVA). The effects of profilin on microtubule polymerization could be explained by a number of possible mechanisms, including that profilin binds or stabilizes tubulin dimers at growing microtubule ends. To test this hypothesis, we performed fluorescence anisotropy to test for a direct interaction between mApple-profilin and unlabeled tubulin dimers. Fluorescent profilin indeed directly bound to tubulin dimers ($k_D = 1.7 \pm 2.0$ µM) (Figure 5G). This binding constant, in the micromolar range, is much less than the physiological concentration of profilin or tubulin. Furthermore, profilin binds the sides of microtubules with much lower affinity ($k_D = \sim 10$ µM; Henty-Ridilla et al., 2017). This result supports the idea that profilin-enhanced microtubule polymerization occurs by orienting or stabilizing tubulin dimer addition to polymerizing microtubules.

We next tested whether specific regions, particularly the growing ends of microtubules, were enriched with mApple-profilin to facilitate polymerization. We performed two-color single-molecule TIRF microscopy and directly observed mApple-profilin and polymerizing microtubules (Figure 5H). A substantial amount mApple-profilin stuck to the imaging surface or was diffusely localized in the imaging plane. Fluorescent profilin was not enriched on the growing ends of microtubules. However, mApple-profilin bound and diffused along the microtubule lattice (Figures 5H-J). The observed profilin-microtubule side-binding interactions were extremely transient. Therefore, these results may not completely rule out profilin binding to the growing ends of microtubules to deposit dimers or stabilize tubulin dimers on growing protofilaments at timescales or resolution below our detection in these experiments. These results further support the idea that a fraction of available profilin is associated with the microtubule cytoskeleton. This suggests a mechanism where profilin accelerates microtubule polymerization by directly binding to tubulin dimers to promote microtubule assembly and then diffusing along the sides of the microtubule lattice to further stabilize microtubule growth.

Profilin regulates the morphology of N2a cells through actin and microtubule crosstalk.

To investigate whether our modified mApple-profilin could replace endogenous profilin in cells, we generated two clonal CRISPR/Cas9 knockout cell lines for profilin-1 in Neuroblastoma-2a (N2a) cells (Figure 6). We used quantitative western blots to determine the level of endogenous

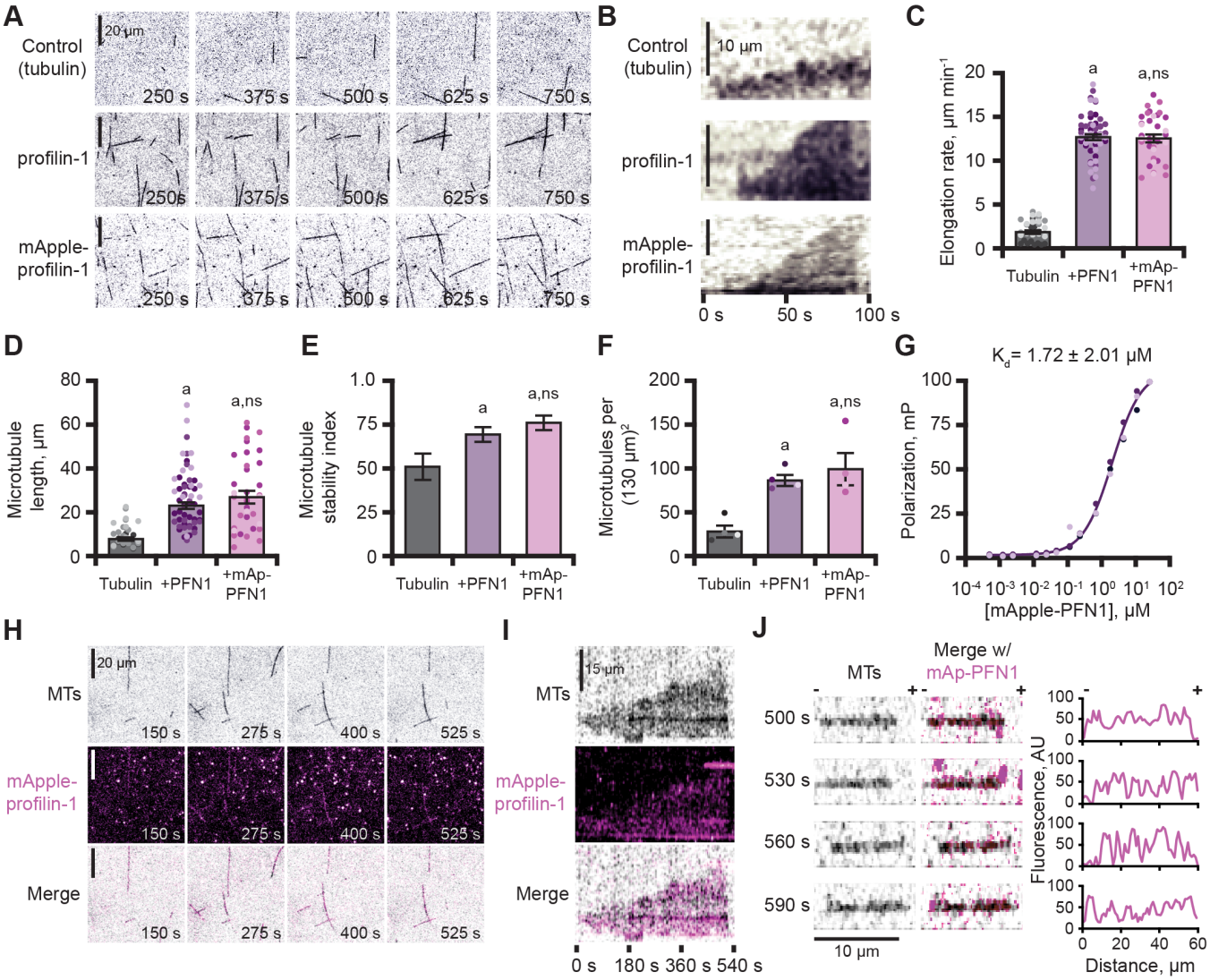

Fig. 5. Profilin binds tubulin dimers and diffuses along the microtubule lattice. (A) Representative views from TIRF reactions containing biotinylated GMP-CPP microtubule seeds, 10 µM free tubulin (5% Alexa-488-labeled) in the absence (control) or presence of 5 µM profilin or 5 µM mApple-profilin. Scale bars, 20 µm. See Supplemental Movie 5. **(B)** Kymographs from reactions as in (A) showing the growth of microtubules. Length scale bars, 10 µm. Elapsed time, 100 s. **(C)** Microtubule elongation rates measured in TIRF assays as in (A) (n = 35-58 microtubules). **(D)** Maximum length to which microtubules grew before undergoing catastrophe in TIRF assays as in (A) (n = 35-58 microtubules). **(E)** Microtubule stability index: rescue/catastrophe frequency (measured from n = 18-46 microtubules). **(F)** Total number of microtubules present in reactions as in (A) (n = 4 independent experiments). Shaded values represent the individual data points used to determine the mean from (n = 3) independent experiments. Error bars indicate SE. **(G)** Fluorescence anisotropy measurement of 10 nM unlabeled tubulin mixed with increasing concentrations of mApple-profilin. **(H)** Two-color views from TIRF reactions containing biotinylated GMP-CPP microtubule seeds, 10 µM free tubulin (5% Alexa-488-labeled) (black), and 5 µM mApple-profilin (pink). Scale bars, 20 µm. See Supplemental Movie 6. **(I)** Kymographs from two-color TIRF reactions as in (H) showing the growth of microtubules (MT). Scale bar, 15 µm. Elapsed time, 540 s. **(J)** Two-color montage of a single microtubule (black) and transiently bound mApple-profilin (pink) on the microtubule lattice. Fluorescence intensity profile from line scans along the microtubule from the mApple-profilin channel. + and - indicate the microtubule polarity. Scale bars, 10 µm. See Supplemental Movie 7. Significant differences by one-way ANOVA with Bartlett's correction for variance: ns, not significantly different from tubulin alone control; a, compared with control ($p < 0.05$); b, compared with untagged profilin (PFN1) ($p < 0.05$).

profilin as well as levels of profilin in CRISPR knockout cells following transfection with plasmids containing untagged profilin, mApple-profilin, or Halo-profilin (Figure 6A). Each CRISPR-generated profilin-deficient cell line proliferated significantly less efficiently than cells with endogenous profilin levels (Figure 6B), likely due to reported defects in the cell cycle (Suetsugu et al., 1998; Witke et al., 2001; Moens and Coumans, 2015). We performed quantitative western blot analysis to assess the efficiency of our rescue experiments. N2a cells contain 121 ± 15 μM profilin-1 (Figure 6C) and various rescue plasmids restored profilin protein to endogenous levels (Figures 6D-6E).

To confirm whether mApple-profilin could fully replace endogenous profilin in cells, we measured N2a cell morphology. We chose this parameter because N2a cells have unique actin filament and microtubule cytoskeletal features but do not efficiently perform other classic cell processes that require intact cytoskeletal crosstalk (i.e., migration or division). We plated N2a cells on Y-shaped micropatterns to standardize cell shape and used super resolution confocal microscopy to image fixed cells. Cells lacking profilin ($PFN1^{-/-}$) displayed aberrant morphologies significantly different from cells with endogenous or rescued profilin levels (Figure 6F). We created an overlay of binarized maximum intensity projections from each cell condition and quantified differences as the cell morphology index (the ratio of endogenous cell area to other cell conditions) to emphasize that the condition of profilin does affect the cellular structure and function (Figure 6G). $PFN1^{-/-}$ cells had significantly altered cell morphology compared to endogenous or mApple-profilin rescue cells ($p < 0.0001$) (Figure 6F and 6G). However, $PFN1^{-/-}$ cells transfected with a plasmid harboring mApple-profilin exhibited morphologies not significantly different from wild-type ($p = 0.99$) (Figures 6F and 6G). We also stained these cells for actin filaments (Figures 6H and 6I) and microtubules (Figure 6J and 6K) and used a similar morphology parameter to detect broad differences in cytoskeletal architecture. Unsurprisingly, the $PFN1^{-/-}$ cells had strikingly aberrant actin filament ($p = 0.0008$) and microtubule networks ($p = 0.0006$) compared to cells with endogenous profilin levels (Figures 6H-6K). Regardless of cytoskeleton, $PFN1^{-/-}$ cells transfected with mApple-profilin displayed morphologies not significantly altered from wild-type $PFN1^{+/+}$ cells ($p = 0.98$) (Figures 6H-6K). Thus, our in vivo observations suggest that mApple-profilin is functional for cytoskeleton-based activities in cells.

Discussion

The lipid, actin, and microtubule regulating capabilities of profilin position it as a critical convergence point at the interface of major cell signaling pathways. However, the physiological significance for these findings have not been fully elucidated as previous methods used to tag profilin compromise different aspects of its function. Direct labeling approaches require several mutations and result in profilin aggregation (Vinson et al., 1998; Henty-Ridilla et al., 2017). Tagging directly on the C- or N-terminus disrupts PLP-binding (Wittenmayer et al., 2000). Splitting profilin to insert a fluorescence tag at a protruding loop in its tertiary structure results in a fusion protein that binds PLP and lipids with native affinity, but compromises actin binding (Nejedla et al., 2017). High cellular concentrations of profilin (121 μM) further complicate physiological studies attempting to localize profilin in specific signaling schemes. As a consequence, the physiological roles of profilin have been largely understudied. Here we engineered a fluorescently-labeled profilin that binds PIP lipids, actin-monomers, and the PLP-motif containing formin protein. Labeled profilin suppresses spontaneous actin filament nucleation and stimulates formin-based actin polymerization at levels equivalent to untagged profilin. Using this tool, we unambiguously demonstrate that profilin is capable of directly binding to tubulin dimers and to the sides of growing microtubules, stimulating microtubule nucleation and elongation rates. Our genetic analyses in mammalian cells indicate that mApple-profilin and Halo-profilin are fully interchangeable with the endogenous version. These data support a model where profilin mediates interactions between microtubule and actin systems at the level of individual cytoskeletal protein building blocks (i.e., actin monomers and tubulin dimers) (Figure 6L).

Profilin directly interacts with membranes through specific phosphoinositide lipids to modulate cellular actin and microtubule dynamics (Sun et al., 2013; Pinto-Costa and Sousa, 2019; Davey and Moens, 2020). $PI(4,5)P_2$ is the predominant signaling lipid present in cells, and it recruits profilin (and profilin ligands including formin and tubulin) directly to the plasma membrane (Popov et al., 2002; Janmey et al., 2018; Davey and Moens, 2020). Binding of actin or proline-rich ligands release profilin from $PI(4,5)P_2$ present in plasma membrane to regulate cell signaling pathways (Lambrechts et al., 2002; Krishnan and Moens, 2009). $PI(3,5)P_2$ is a low abundance PIP localized on late endosomes and lysosomes (Davey and Moens, 2020). It is considered a critical convergence point between intracellular membrane dynamics, signal transduction, and the cytoskeleton (Ikonomov et al., 2006; Michell et al., 2006). Our tagged versions of profilin maintain full binding capacity for $PI(4,5)P_2$ and $PI(3,5)P_2$ lipids (Figure 2E), which is a critical facet of cellular signal transduction cascades involving profilin in several human diseases including Charcot-Marie-Tooth, amyotrophic lateral sclerosis (ALS), and cancers (Bolino et al., 2000; Pimm et al., 2020).

Profilin is a classic inhibitor of spontaneous actin formation, thus blocking actin assembly through steric interactions (Cooper et al., 1984; Ferron et al., 2007). Additionally, in vitro studies revealed a fierce competition among actin filament nucleation systems (i.e., formins, Ena/VASP, or the Arp2/3 Complex) for profilin-bound actin monomers to ultimately dictate whether linear or branched actin networks are formed (Rotty et al., 2015; Suarez et al., 2015). Genetic studies in yeast further corroborated these competitive internetwork dynamics (Suarez and Kovar, 2016). However, yeast lack thymosin-β4, a high affinity ligand that outcom-

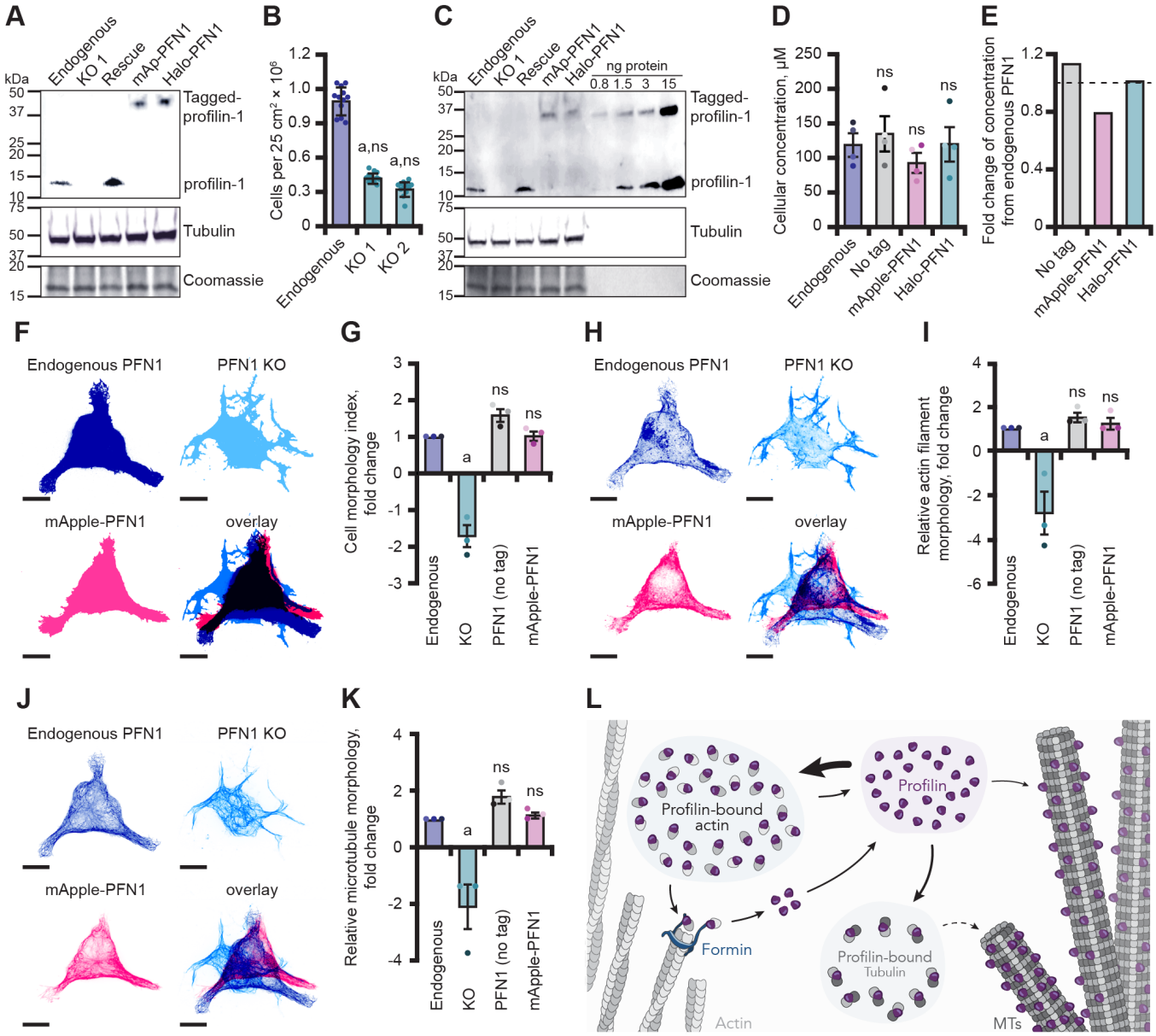

Fig. 6. Tagged profilin rescues cell morphology phenotypes present in profilin-deficient cells. (A) Western blot confirming CRISPR knockout and rescue of profilin-1 with either mAp-PFN1 or Halo-PFN1 constructs. N2a cell extracts were prepared from wild-type N2a (PFN1$^{+/+}$), profilin knockout (PFN1$^{-/-}$), or profilin knockout cells 24 h after transfection with a tag-less rescue construct, mAp-PFN1, or Halo-PFN1. Blots were probed with Profilin-1 B 10 primary (1:3,500 dilution; SantaCruz 137235) and goat anti-mouse 926-32210 secondary (1:5,000 dilution; LI-COR Biotechnology) antibodies. α-tubulin primary (1:10,000; Abcam 18251) and donkey anti-rabbit 926-68073 secondary (1:20,000) and the Coomassie stained membrane were used as a loading control. **(B)** Profilin-deficient cells proliferate less efficiently than wild-type controls. **(C)** Representative blot used to determine the concentration of endogenous profilin-1 in Neuroblastoma-2a (N2a) cells. Blot was probed as in (A) compared to known quantities of purified mApple-profilin (43 kDa) or untagged profilin (15 kDa). Images of full blots are present in Figure S6. **(D)** Cellular concentration of endogenous profilin or several profilin rescue constructs (untagged, mApple-, or Halo-tags). Concentration was calculated from 100,000 cells and the volume of an N2a cell that we calculated as 196 (µm3) similar to (Cadart et al., 2017). Mean values from four independent experiments ± SE shown. **(E)** Fold-change in profilin levels in PFN1$^{(-/-)}$ cells transfected with tagged or untagged profilin plasmids. Each construct rescues profilin protein levels to endogenous levels. **(F)** Super resolution confocal imaging of wild-type (endogenous; blue), profilin knockout (PFN1$^{(-/-)}$; cyan), or PFN1$^{(-/-)}$ transfected with mApple-PFN1 (pink) cells plated on Y micropatterns. N2a cells are shown individually and as an overlay aligned by the micropattern. **(G)** Quantification of cell morphology, calculated as a ratio of cell area to endogenous control cells from images similar to (F). PFN1$^{(-/-)}$ cells displayed significantly aberrant morphology, cells rescued with mApple-profilin plasmid were not significantly different compared to endogenous controls (PFN1$^{(+/+)}$). **(H)** Phalloidin-stained actin filaments from cells in (F). **(I)** Quantification of actin morphology of N2a cells plated similarly to (F). Actin morphology calculated from actin filament signals similar to the cell morphology index, above (G). **(J)** Tubulin immunofluorescence in the same N2a cells as in (F). α-tubulin was stained with 1:100 primary (Abcam 18251) and 1:100 fluorescently conjugated donkey anti-rabbit AlexaFluor-647 secondary (A31573; Life Technologies) antibodies. **(K)** Quantification of microtubule morphology of N2a cells plated similarly to (F). Error bars indicate SE. Significant differences by one-way ANOVA with Bartlett's correction for variance: ns, not significantly different from endogenous PFN1$^{(+/+)}$ control; a, compared with control ($p < 0.05$). Scale bars, 10 µm. **(L)** Model for profilin distribution between actin and microtubules. Actin monomers, actin filament nucleators (i.e., formin or Ena/VASP), microtubules, and tubulin dimers all compete for free profilin in a cell. This competition dictates higher-order actin-microtubule crosstalk in cells.

petes profilin for actin monomers (20-fold higher affinity) (Figure 3A; Jean et al., 1994; Skruber et al., 2018; Pimm et al., 2020). Elegant work precisely tuning the concentrations of profilin in mammalian cells resulted in polymerization of discrete actin networks at the leading edge (Skruber et al., 2020). Given the presence of PI(4,5)P_2 at the plasma membrane, the preferred mechanism of actin assembly in cells is profilin-dependent, using formin proteins (Suarez et al., 2015; Funk et al., 2019; Skruber et al., 2020). Our functional labeled profilin may allow for direct visualization of this dynamic competition and collaboration between actin filament nucleation systems.

Many cell processes that rely on the functional interplay between actin and microtubules are also mediated through profilin (Pinto-Costa and Sousa, 2019; Davey and Moens, 2020; Pimm et al., 2020; Karlsson and Dráber, 2021; Pimm and Henty-Ridilla, 2021). Profilin colocalizes to the sides of microtubules in several cell types (Di Nardo et al., 2000; Grenklo et al., 2004; Nejedla et al., 2016). Profilin is also present at centrosomes in B16 cells bound to the microtubule nucleation complex γ-TuRC (Consolati et al., 2020; Karlsson and Dráber, 2021; Nejedlá et al., 2021). Depending on the cell type, overexpression of profilin stimulates the mean growth rate of cellular microtubules up to 5-fold (Nejedla et al., 2016; Henty-Ridilla et al., 2017). Based on localization experiments using the pan-formin inhibitor, SMIFH2, some interactions between profilin and the sides of microtubules are thought to be indirect (Nejedla et al., 2016; Nejedlá et al., 2021). However, recent studies suggest SMIFH2 treatments disrupt other critical cytoskeletal regulation proteins (i.e., myosins and p53) in addition to formins (Isogai et al., 2015; Nishimura et al., 2021). Using fluorescent profilin we learned that in addition to binding the sides of microtubules, profilin also directly binds tubulin dimers (Figure 5G). With this evidence in mind, an attractive model to explain how profilin enhances microtubule polymerization is that the higher affinity of mApple-profilin for tubulin dimers (K_D = 1.7 μM) and more efficiently organizes dimer addition to microtubules. This may accelerate microtubule assembly from protofilaments or at microtubule plus-ends. Once assembled, profilin may remain associated with the microtubule lattice to stabilize lateral contacts along the microtubule lattice. This may also confirm the hypothesis that profilin lowers the critical concentration required for microtubule assembly (Henty-Ridilla et al., 2017; Nejedlá et al., 2021). Future studies may combine this labeling (mApple- or Halo-tag titration; Figure 6) strategy with specific actin- or microtubule-polymerization disrupting point mutations to decipher the factors that result in the formation of diverse actin or microtubule arrays.

Methods

Reagents.

All materials were obtained from Fisher Scientific (Waltham, MA) unless otherwise noted.

Plasmid construction.

Purified DNA from a vector containing full-length mApple (mApple-C1 vector; Kremers et al., 2009) was PCR amplified with the following primers to generate overlapping ends: forward: 5'-CTTTAAGAAGGAGATATACATATGGTGAGCAAGGGCGAGG-3'; and, reverse: 5'- CCACCCGGCCATGGAAGCTTGAGC -3'. DNA fragments of full-length mApple containing overlapping ends and NdeI-linearized pMW172 containing the full-length sequence of human profilin-1 (NCBI Gene ID: 5216; Eads et al., 1998; Henty-Ridilla et al., 2017) were joined via Gibson assembly according to manufacturer's instructions (NEB, Ipswich, MA). The final cassette is an N-terminal mApple fluorescent protein, followed by a ten amino acid spacer, and profilin-1, that is flanked by NdeI and EcoRI restriction sites. Mammalian expression vectors were generated by Genscript (Piscataway, NJ) as follows: the mApple-Profilin cassette was synthesized and inserted into the backbone of mApple-C1 behind the CMV promoter at the Ndel and BamHI restriction sites, replacing the original mApple sequence; For Halo-profilin, the ten amino acid linker and profilin-1 was synthesized and inserted into the backbone of a pcDNA-Halo expression vector (provided by Gunther Hollopeter, Cornell University) at the KpnI and NotI restriction sites. The final sequence for each plasmid constructed above was verified by Sanger sequencing (Genewiz, South Plainfield, NJ).

Protein purification.

Profilin constructs (wild-type or mApple-profilin) were transformed and expressed in Rosetta2(DE3) (Millipore-Sigma, Burlington, MA) competent cells. Cells were grown in Terrific Broth to OD600 = 0.6 at 37 °C, then induced with IPTG for 18 h at 18 °C. Cells were collected by centrifugation and stored at -80 °C until purification. Cell pellets were resuspended in 50 mM Tris HCl (pH 8.0), 10 mg/mL DNase I, 20 mg/mL PMSF, and 1× protease inhibitor cocktail (0.5 mg/mL Leupeptin, 1000 U/mL Aprotinin, 0.5 mg/mL Pepstatin A, 0.5 mg/mL Antipain, 0.5 mg/mL Chymostatin). Cells were incubated with 1 mg/mL lysozyme for 30 min and then lysed on ice with a probe sonicator at 100 mW for 90 s. The cell lysate was clarified by centrifugation at 278,000 × g. The supernatant was passed over a QHighTrap column (Cytiva, Marlborough, MA) equilibrated in 50 mM Tris-HCl (pH 8.0), 1 M KCl. Profilin was collected in the flow through and then applied to a Superdex 75 (10/300) gel filtration column (Cytiva) equilibrated in 50 mM Tris (pH 8.0), 50 mM KCl. Fractions containing profilin were pooled, aliquoted, and stored at 80 °C.

N-terminally tagged 6×His-GFP-thymosin-β4 (GFP-Tβ4) was synthesized and cloned into a modified pET23b vector at the AgeI and NotI restriction sites (Genscript). Bacteria were transformed, induced, collected, and stored as described for profilin (above). Cell pellets were resuspended in lysis buffer (2× PBS (pH 8.0) (2.8 M NaCl, 50 mM KCl, 200 mM sodium

dibasic, 35 mM potassium monobasic), 20 mM Imidazole (pH 7.4), 500 mM NaCl, 0.1 % Triton-X 100, 14 mM BME) and lysed as above. Lysate was clarified via centrifugation for 30 min at 20,000 x g and the supernatant was flowed over Cobalt affinity columns (Cytiva) equilibrated in low imidazole buffer (1× PBS (pH 8.0) supplemented with 20 mM Imidazole (pH 7.4), 500 mM NaCl, 0.1% Triton-X 100, 14 mM BME). GFP-Tβ4 was eluted using a linear gradient into high imidazole buffer (1× PBS (pH 8.0) supplemented with 300 mM Imidazole (pH 7.4), 150 mM NaCl, 0.1% Triton-X 100, 14 mM BME) and the 6×His-tag was cleaved with 5 mg/mL ULP1 protease for 2 h at 4 °C, concentrated, and applied to a Superdex 75 (10/300) gel filtration column equilibrated with GF buffer (1× PBS (pH 8.0) supplemented with 150 mM NaCl, 14 mM BME). Fractions containing GFP-Tβ4 were pooled, aliquoted and stored at -80 °C.

The constitutively active formin 6×His-mDia1(FH1-C) (amino acids 571-1255) was synthesized and cloned into modified pET23b vector at the AgeI and NotI restriction sites (Genscript). Bacteria were transformed, induced, and collected as described for profilin and GFP-Tβ4. The protein was purified as described for GFP-Tβ4, with the exception of applying the cleaved formin to a Superose 6 Increase (10/300) gel filtration column (Cytiva). Fractions containing mDia1(FH1-C) were pooled, aliquoted, and stored at -80 °C.

Rabbit skeletal muscle actin (RMA), Oregon-Green (OG) labeled-actin, and N-(1-pyrenyl)iodoacetamide (pyrene) actin were purified from acetone powder as described in detail (Spudich and Watt, 1971; Cooper et al., 1984; Henty-Ridilla et al., 2017), however rather than starting with frozen tissue, fresh rabbit muscle (Side Hill Farmers, Manlius, NY) was used. Alexa-647-actin was labeled on lysine residues as follows: 5 g of acetone powder was rehydrated in G-buffer (3 mM Tris pH 8.0, 0.5 mM DTT, 0.2 M ATP, 0.1 mM $CaCl_2$) for 60 min on ice. Actin was polymerized from the supernatant overnight at 4 °C with the addition of 2 mM $MgCl_2$, 50 mM NaCl and 0.5 mM ATP. The following day, the concentration of NaCl was adjusted to 0.6 M, the polymerized actin was collected by centrifugation at 361,000 × g, and then depolymerized by dounce homogenization and dialysis against G-buffer for 24 h at 4C. Dialysis buffer was replaced with labeling buffer (100 mM PIPES-Tris (pH 6.8), 100 mM KCl, 0.4 mM ATP, 0.4 mM $CaCl_2$) for 2 h at 4 °C and exchanged twice. Dialyzed actin was polymerized by adding 1 mM $MgCl_2$ and 50 mM KCl and labeled with a 5-20-fold excess of NHS-Alexa-647 for 18 h at 4 °C. Labeled actin filaments were depolymerized by dounce homogenization and dialysis as above, precleared at 435,000 × g, and loaded onto a HiPrep S200 (16/60) gel filtration column (Cytiva) equilibrated in G-Buffer. Fractions containing labeled actin were pooled and dialyzed against G-buffer supplemented with 50% glycerol and stored at 4 °C. All purified actins were pre-cleared at 279,000 × g before use.

Tubulin was purified from freshly obtained Bovine brains by three cycles of temperature-induced polymerization and depolymerization as described in detail (Castoldi and Popov, 2003). Fluorescently labeled tubulin was purchased from Cytoskeleton, Inc (Denver, CO), and resuspended according to manufacturer's instructions. AlexaFluor-647 GMP-CPP microtubule seeds were polymerized by combining 15 µM unlabeled tubulin, 7.5 µM AlexaFluor-647 tubulin, 7.5 µM biotin-tubulin, and 0.5 mM GpCpp (Jena Bioscience, Jena, Germany) and incubating for 30 min at 37 °C (Groen et al., 2014). Seeds were collected by centrifugation and resuspended in 1×BRB80 (80 mM PIPES, 1 mM $MgCl_2$, 1 mM EGTA, pH 6.8 with KOH), aliquoted, and stored at 80 °C. Unlabeled tubulin was recycled before use in TIRF microscopy assays (Castoldi and Popov, 2003).

All protein concentrations were determined by band densitometry from Coomassie-stained SDS-PAGE gels, compared to a BSA standard curve. Band intensities were quantified using a LI-COR Odyssey imaging system (LI-COR Biotechnology, Lincoln, NE). Labeling stoichiometries were determined using the spectroscopy, molar extinction coefficients, and predetermined correction factors, as follows: unlabeled actin ε_{290} = 25,974 M^{-1} cm^{-1}, Oregon Green ε_{496} = 70,000 M^{-1} cm , Alexa-650 = 239,000 . The correction factor used for Oregon Green was 0.12, and for Alexa-647 was 0.03.

Liposome preparation and pelleting assays.

Liposomes (Avanti Polar lipids, Alabaster, AL) of defined PIP lipid content were prepared according to (Banerjee and Kane, 2017). Briefly, powdered lipids were resuspended in CH_3OH:$CHCl_3$:H_2O at a 9:20:1 ratio. Liposomes contained 55% (mol %) 16:0 phosphatidylcholine, 25% 16:0 phosphatidylserine (PS), 18% 16:0 phosphatidylethnolamine, and 5% 18:1 (0.33 mM final concentration) phosphatidylinositol phosphates (PI(3,5)P_2 or PI(4,5)P_2). Control liposomes did not contain PIPs but did contain 16:0 phosphatidylserine. The mixed lipids were dried using a centrivap lyophilizer with a vacuum pump at 35 °C for 30–40 min. Lyophilized lipids were resuspended and in ice-cold liposome buffer (25 mM NaCl, pH 7.4, 50 mM Tris-HCl), and then subjected to five freeze-thaw cycles. Finally, liposomes were extruded through a 100 nm filter 20 times. 1 µM profilin (untagged or mApple-profilin) was mixed with 0.33 mM PIP liposomes in resuspension buffer (50 mM Tris, pH 8.0; 150 mM KCl; 10 mM DTT). The solution was incubated at room temperature for 30 min, then liposomes were pelleted via centrifugation at 400,000 × g for 30 min. The supernatant and pellet fractions were separated and then the pellet was resuspended in an equal volume (i.e., 100 µL) of buffer. Samples were precipitated using 10%(v/v) trichloroacetic acid, washed with cold acetone, and dissolved in 50 µL of cracking buffer (50 mM Tris-HCl, pH 6.8, 8 M urea, 5% SDS, and 1 mM EDTA). Each sample was separated by SDS-PAGE electrophoresis and transferred into nitrocellulose membrane. The resulting blots were probed with 1:5,000 profilin-1 anti-mouse 137235 primary (SantaCruz Biotechnology, Dallas, TX) and 1:10,000 IRDye 800 Goat anti-mouse 926-32210 secondary (LI-COR Biotechnology, Lincoln, NE) antibodies. Antibodies recognizing profilin

were detected using a LI-COR Odyssey Fc imaging system and quantified by densitometry in Fiji (Schindelin et al., 2012).

Fluorescence anisotropy binding assays.

Direct actin-binding experiments were performed in binding mix (1× PBS (pH 8.0) supplemented with 150 mM NaCl). Reactions with actin (10 nM) (unlabeled or OG-labeled) were incubated at room temperature for 15 min and anisotropy was determined by exciting at 440 nm and measuring emission intensity at 510 nm with bandwidths set to 20 nm using a Tecan plate reader (Tecan, Männedorf, Switzerland) equipped with a monochromator. Competitive actin-binding experiments contained 10 nM unlabeled actin and 10 nM GFP-Tβ4 with variable concentrations of unlabeled profilin or mApple-profilin. Direct binding analyses utilizing mApple-profilin (various concentrations) were measured using 568 nm excitation and 592 nm emission with bandwidths set to 20 nm. Direct tubulin-binding experiments were performed with 10 nM tubulin in 1×BRB80 supplemented with 150 mM NaCl. Reactions were incubated at 4 °C for 30 min before reading. Reactions containing tubulin were screened for the presence of microtubules at the conclusion of the experiment. No microtubules were present in any condition. Reactions with all proteins were precleared via centrifugation at 279,000 × g before use.

Bulk actin assembly assays.

Bulk actin assembly assays were performed by combining freshly Mg-ATP recycled 2 µM monomeric actin (5% pyrene labeled), proteins or control buffers, and initiation mix (2 mM $MgCl_2$, 0.5 mM ATP, 50 mM KCl). Reactions for each replicate were initiated simultaneously by adding actin to reactions using a multichannel pipette. Total fluorescence was monitored using excitation 365 nm and emission 407 nm in a Tecan plate reader. Recorded values were averaged between three replicates. Shaded areas represent the standard deviation between replicates.

In vitro TIRF microscopy assays.

TIRF microscopy flow cells were prepared by attaching PEG-silane coated coverslips to µ-Slide VI0.1 (0.1 mm × 17 mm × 1 mm) flow chambers (Ibidi, Martinsried, Germany) with 120 µm thick double-sided tape (2.5 cm × 2 mm × 120 µm) (Grace Bio-Labs, Bend, OR) and 5-minute epoxy (Devcon, Riviera Beach, FL) (Smith et al., 2013). Imaging chambers were conditioned as follows: 1% BSA, 4 µg/mL streptavidin in 10 mM Tris-HCl (pH 8.0), 1% BSA, and then 1× TIRF buffer supplemented with 0.25% methylcellulose [4000 cP] for actin (20 mM imidazole (pH 7.4) 50 mM KCl, 1 mM $MgCl_2$, 1 mM EGTA, 0.2 mM ATP, 10 mM DTT, 40 mM glucose) or microtubules (1× BRB80, 50 mM KCl, 0.1 mM GTP, 10 mM DTT, 40 mM glucose). Time lapse TIRF microscopy was performed using a DMi8 inverted microscope equipped with 120-150 mW solid-state lasers, a 100× Plan Apo 1.47 N.A. oil-immersion TIRF objective (Leica Microsystems, Wetzlar, Germany), and an iXon Life 897 EMCCD camera (Andor; Belfast, Northern Ireland). Focus was maintained using the adaptive focus system (Leica Microsystems, Wetzlar, Germany), and frames were captured at 5 s intervals. Reactions visualizing actin used 50 ms exposure, 488 nm or 647 nm excitations. For microtubules settings were 100 ms exposure, 488 nM excitation, 10% laser power. Reactions visualizing mApple-profilin used 100 ms exposure, 561 nM excitation, with 5% laser power. Reactions were introduced into the flow chamber using a luer lock system on the coverslip directly mounted on the microscope stage, and flow was achieved with a syringe pump (Harvard Apparatus, Holliston, MA). All reactions are timed from the initial mixing of proteins rather than the start of image acquisition (usually delayed by 15-20 s). Reactions containing actin were performed at room temperature. Reactions with growing microtubules were performed at 35 °C, maintained by a stage and objective heater system (OKO lab, Pozzuoli, Italy). Actin and microtubules were loosely tethered to the cover glass surface using an avidin-biotin conjugation system. Dynamic parameters for actin or microtubules were determined by analyzing TIRF movies in Fiji (Schindelin et al., 2012). Actin nucleation was measured as the number of actin filaments present 100 s after the initiation of the reaction. Actin filament elongation rates were measured as the slope of a line generated from the length (µm) of actin filaments over time for at least four consecutive movie frames. This number was multiplied by the number of actin subunits per micron, previously calculated as 370 subunits (Pollard et al., 2000). Microtubule length measurements and elongation rates (microns per min) were determined from kymographs as the change in microtubule length divided by time spent growing. Microtubule stability index was calculated as the ratio of catastrophe events divided by the number of rescue events.

Mammalian cell culture, confocal microscopy, and imaging analysis.

Neuroblastoma (N2a) cells were grown in DMEM supplemented with 200 mM L-glutamine, and 10% FBS. Transfections were performed using Lipofectamine 3000 according to manufacturer's instructions for 6-well plates using 75,000 cells and 100-200 ng plasmid per well. Cells were lysed (for western blots) or imaged 18-24 h following transfection. Pooled profilin-1 CRISPR and comparable wild-type N2a cells (Synthego, Menlo Park, CA) were diluted to an average of 0.5 cells per well and further screened via western blot for clonal profilin-1 knockout lines using identical conditions as described for quantitative western blots, below. For cell counts, wild-type and profilin knockout cells were seeded at 100,000 cells per T25 flask (Genesee Scientific, San Diego, CA), passaged, and counted every 4 d.

100,000 cells were plated on medium-sized fibronectin coated Y-patterned coverslips (CYTOO, Grenoble, France).

After 4 h unbound cells were aspirated, and remaining attached cells were fixed in 8% glutaraldehyde diluted in 1x PBS. Autofluorescence was quenched with freshly prepared 0.1%(w/v) sodium borohydride. Microtubules were visualized by immunofluorescence as follows. Fixed cells were permeabilized in 1× PBS supplemented with 0.25% Triton X-100, blocked for 1 h in 1% BSA (w/v) diluted in PBST (1× PBS supplemented with 0.1% Tween (v/v)) and incubated with 1:250 anti-rabbit primary antibody 18251 against α-tubulin (Abcam, Cambridge, UK) for 16 h. Coverslips were washed with 1× PBST and incubated for 1 h with a combination of: 1:500 donkey anti-rabbit secondary antibody AlexaFluor-568 and 1:500 AlexaFluor-647 phalloidin to stain actin filaments. Coverslips were mounted in AquaMount.

Fixed cells were imaged by spinning disc confocal microscopy on an inverted Nikon Ti2-E microscope (Nikon Instruments, Melville, NY) equipped with a compact 4-line laser source (405 nm, 488 nm, 561 nm, and 640 nm wavelengths), a CF160 Plan Apo 60× 1.4 N.A. oil-immersion objective, a CSU-W1 imaging head (Yokogawa Instruments, Tokyo, Japan), a SoRa disc (Nikon Instruments, Melville, NY), and a Prime BSI sCMOS camera with a pixel size of 6.5 µm/pixel (Teledyne Photometrics, Tucson, AZ). Images were acquired using Nikon Elements software with artificial intelligence analysis modules. Maximum intensity projections and fluorescence subtraction for cell, actin, and microtubule morphologies was performed using Fiji (Schindelin et al., 2012). Briefly masks of wild-type cells were aligned by the micropattern shape and overlaid on profilin knockout or profilin-1 knockout cells expressing tagged and untagged profilin expression plasmids. Mean ratios from three different coverslips are shown.

Determination of cellular profilin concentrations.

The concentration of profilin, mApple-profilin, or Halo-profilin in N2a cells was determined using quantitative western blots. 100,000 cells were seeded and then grown to confluency in 6-well plates and lysed in equal volumes of 2× Laemmli buffer. Equal volumes of cell lysate per condition were loaded on SDS-PAGE gels alongside a profilin standard curve. Lysates were not corrected for transformation efficiency. However, transformation efficiencies were typically between 70-90% of the total cells plated. Blots were probed with a 1:3500 dilution of profilin-1 anti-mouse 137235 primary antibody (Santa Cruz Biotechnology, Inc.) for 16 h. Blots were washed three times and probed with 1:6000 IRDye 800 Goat anti-mouse 926-32210 secondary antibody (LI-COR Biotechnology) for 1 h at room temperature and washed again. Fluorescent secondary antibodies recognizing profilin were detected using a LI-COR Odyssey Fc imaging system and quantified by densitometry in Fiji (Schindelin et al., 2012). The amount of profilin was determined by comparing levels to the standard curve. Values were averaged from four independent blots. The mean cell volume of a typical N2a cell was calculated as 196 μm^3 (1.96 × 10-13 L) by taking the average XY area of ten well-spread N2a cells and then multiplying by the mean cell thickness in Z (1 µm) from the same cells, similar to (Christ et al., 2010; Cadart et al., 2017).

Data analyses and availability.

GraphPad Prism 9 (GraphPad Software, San Diego, CA) was used for all data analyses and to perform all statistical tests. Non-linear curve fits for anisotropy experiments were performed using data normalized so that the smallest mean in each data set was defined as zero. Data was fit to the following curve using least squares regression with no constraints: $Y = Y_0\text{-Bmax}*(X/(KD+X))$. The specific details for each experimental design, sample size, and specific statistical tests are available in the figure legends. P-values lower than 0.05 were considered significant for all analyses. Individual data points are included for each figure. Different shades of data points show technical replicates. All experiments were performed at least three times.

Datasets for each figure have been deposited in the Zenodo Henty-Ridilla laboratory community available, here: http://doi.org/10.5281/zenodo.5329585. Access will be granted upon reasonable request.

Supplemental information

Supplemental information includes 6 figures and 7 movies.

Author contributions

M.L.P, X.L., F.T., and J.L.H-R performed the experiments. M.L.P, X.L., A.L., F.T., and J.L.H-R analyzed the experiments. J.L.H-R designed experiments, supervised, and obtained funding for this work. J.L.H-R wrote the manuscript.

Competing interests

The authors declare no competing interests.

Acknowledgements

We are grateful to Marc Ridilla (Repair Biotechnologies) and Brian Haarer (SUNY Upstate) for comments on this manuscript. This research was funded by a Sinsheimer Scholar Award, Amyotrophic Lateral Sclerosis Association Starter Grant (20-IIP-506), and NIHR35 GM133485.

References

1. Aguda, AH, Xue, B, Irobi, E, Préat, T, and Robinson, RC (2006). The structural basis of actin interaction with multiple WH2/β-thymosin motif-containing proteins. Structure 14, 469–476.
2. Antoine, M et al. (2020). Splicing defects of the profilin gene alter actin dynamics in an S. pombe SMN Mutant. iScience 23, 100809.

3. Banerjee, S, and Kane, PM (2017). Direct interaction of the Golgi V-ATPase a-subunit isoform with PI(4)P drives localization of Golgi V-ATPases in yeast. Mol Biol Cell 28, 2518–2530.
4. Blanchoin, L, Boujemaa-Paterski, R, Sykes, C, and Plastino, J (2014). Actin dynamics, architecture, and mechanics in cell motility. Physiol Rev 94, 235–263.
5. Bolino, A et al. (2000). Charcot-Marie-Tooth type 4B is caused by mutations in the gene encoding myotubularin-related protein-2. Nat Genet 25, 17–19.
6. Cadart, C, Zlotek-Zlotkiewicz, E, Venkova, L, Thouvenin, O, Racine, V, Le Berre, M, Monnier, S, and Piel, M (2017). Fluorescence eXclusion measurement of volume in live cells. Methods Cell Biol 139, 103–120.
7. Castoldi, M, and Popov, AV (2003). Purification of brain tubulin through two cycles of polymerization-depolymerization in a high-molarity buffer. Protein Expr Purif 32, 83–88.
8. Chandra, M et al. (2019). Classification of the human phox homology (PX) domains based on their phosphoinositide binding specificities. Nat Commun 10, 1528.
9. Chang, F, Drubin, D, and Nurse, P (1997). Cdc12p, a protein required for cytokinesis in fission yeast, is a component of the cell division ring and interacts with profilin. J Cell Biol 137, 169–182.
10. Christ, KV, Williamson, KB, Masters, KS, and Turner, KT (2010). Measurement of single-cell adhesion strength using a microfluidic assay. Biomed Microdevices 12, 443–455.
11. Consolati, T et al. (2020). Microtubule nucleation properties of single human γTuRCs explained by their cryo-EM structure. Dev Cell 53, 603-617.e8.
12. Cooper, JA, Blum, JD, and Pollard, TD (1984). Acanthamoeba castellanii capping protein: properties, mechanism of action, immunologic cross-reactivity, and localization. J Cell Biol 99, 217–225.
13. Courtemanche, N, and Pollard, TD (2013). Interaction of profilin with the barbed end of actin filaments. Biochemistry 52, 6456–6466.
14. Davey, RJ, and Moens, PD (2020). Profilin: many facets of a small protein. Biophys Rev 12, 827–849.
15. DeCaprio, J, and Kohl, TO (2020). Differential detergent lysis of cellular fractions for immunoprecipitation. Cold Spring Harb Protoc 2, 098582.
16. Di Nardo, A, Gareus, R, Kwiatkowski, D, and Witke, W (2000). Alternative splicing of the mouse profilin II gene generates functionally different profilin isoforms. J Cell Sci 113, 3795–3803.
17. Ding, Z, Bae, YH, and Roy, P (2012). Molecular insights on context-specific role of profilin-1 in cell migration. Cell Adh Migr 6, 442–449.
18. Dong, J, Radau, B, Otto, A, Müller, E-C, Lindschau, C, and Westermann, P (2000). Profilin I attached to the Golgi is required for the formation of constitutive transport vesicles at the trans-Golgi network. Biochim Biophys Acta Mol Cell Res 2, 253–260.
19. Eads, JC, Mahoney, NM, Vorobiev, S, Bresnick, AR, Wen, K-K, Rubenstein, PA, Haarer, BK, and Almo, SC (1998). Structure determination and characterization of Saccharomyces cerevisiae profilin. Biochemistry 37, 11171–11181.
20. Evangelista, M, Blundell, K, Longtine, MS, Chow, CJ, Adames, N, Pringle, JR, Peter, M, and Boone, C (1997). Bni1p, a yeast formin linking cdc42p and the actin cytoskeleton during polarized morphogenesis. Science 276, 118–122.
21. Evangelista, M, Pruyne, D, Amberg, DC, Boone, C, and Bretscher, A (2002). Formins direct Arp2/3-independent actin filament assembly to polarize cell growth in yeast. Nat Cell Biol 4, 260–269.
22. Ferron, F, Rebowski, G, Lee, SH, and Dominguez, R (2007). Structural basis for the recruitment of profilin-actin complexes during filament elongation by Ena/VASP. EMBO J 26, 4597–4606.
23. Funk, J, Merino, F, Venkova, L, Heydenreich, L, Kierfeld, J, Vargas, P, Raunser, S, Piel, M, and Bieling, P (2019). Profilin and formin constitute a pacemaker system for robust actin filament growth. Elife 8, e50963.
24. Gertler, FB, Niebuhr, K, Reinhard, M, Wehland, J, and Soriano, P (1996). Mena, a relative of VASP and Drosophila Enabled, is implicated in the control of microfilament dynamics. Cell 87, 227–239.
25. Goldschmidt-Clermont, PJ, Furman, MI, Wachsstock, D, Safer, D, Nachmias, VT, and Pollard, TD (1992). The control of actin nucleotide exchange by thymosin beta 4 and profilin. A potential regulatory mechanism for actin polymerization in cells. Mol Biol Cell 3, 1015–1024.
26. Goldschmidt-Clermont, PJ, Machesky, LM, Baldassare, JJ, and Pollard, TD (1990). The actin-binding protein profilin binds to PIP2 and inhibits its hydrolysis by phospholipase C. Science 247, 1575–1578.
27. Grenklo, S, Johansson, T, Bertilson, L, and Karlsson, R (2004). Anti-actin antibodies generated against profilin:actin distinguish between non-filamentous and filamentous actin, and label cultured cells in a dotted pattern. Eur J Cell Biol 83, 413–423.
28. Groen, AC, Ngyuen, PA, Field, CM, Ishihara, K, and Mitchison, TJ (2014). Glycogen-supplemented mitotic cytosol for analyzing Xenopus egg microtubule organization. Meth Enzymol 540, 417–433.
29. Hartwig, JH, Chambers, KA, Hopcia, KL, and Kwiatkowski, DJ (1989). Association of profilin with filament-free regions of human leukocyte and platelet membranes and reversible membrane binding during platelet activation. J Cell Biol 109, 1571–1579.
30. Henty-Ridilla, JL, and Goode, BL (2015). Global resource distribution: allocation of actin building blocks by profilin. Dev Cell 32, 5–6.
31. Henty-Ridilla, JL, Juanes, MA, and Goode, BL (2017). Profilin directly promotes microtubule growth through residues mutated in amyotrophic lateral sclerosis. Curr Biol 27, 3535-3543.e4.
32. Henty-Ridilla, JL, Rankova, A, Eskin, JA, Kenny, K, and Goode, BL (2016). Accelerated actin filament polymerization from microtubule plus ends. Science 352, 1004-1009.

33. Higgs, HN, and Pollard, TD (1999). Regulation of actin polymerization by Arp2/3 complex and WASp/scar proteins. J Biol Chem 274, 32531–32534.
34. Ikonomov, OC, Sbrissa, D, and Shisheva, A (2006). Localized PtdIns 3,5-P2 synthesis to regulate early endosome dynamics and fusion. Am J Physiol Cell Physiol 291, C393-404.
35. Isogai, T, van der Kammen, R, and Innocenti, M (2015). SMIFH2 has effects on formins and p53 that perturb the cell cytoskeleton. Sci Rep 5, 9802.
36. Janmey, PA, Bucki, R, and Radhakrishnan, R (2018). Regulation of actin assembly by PI(4,5)P2 and other inositol phospholipids: an update on possible mechanisms. Biochem Biophys Res Commun 506, 307–314.
37. Jean, C, Rieger, K, Blanchoin, L, Carlier, MF, Lenfant, M, and Pantaloni, D (1994). Interaction of G-actin with thymosin beta 4 and its variants thymosin beta 9 and thymosin beta met9. J Muscle Res Cell Motil 15, 278–286.
38. Jégou, A, Niedermayer, T, Orbán, J, Didry, D, Lipowsky, R, Carlier, M-F, and Romet-Lemonne, G (2011). Individual actin filaments in a microfluidic flow reveal the mechanism of ATP hydrolysis and give insight into the properties of profilin. PLoS Biol 9, e1001161.
39. Kaiser, DA, Vinson, VK, Murphy, DB, and Pollard, TD (1999). Profilin is predominantly associated with monomeric actin in Acanthamoeba. J Cell Sci 112, 3779–3790.
40. Karlsson, R, and Dráber, P (2021). Profilin-A master coordinator of actin and microtubule organization in mammalian cells. J Cell Physiol 236, 7256–7265.
41. Koestler, SA, Rottner, K, Lai, F, Block, J, Vinzenz, M, and Small, JV (2009). F- and G-actin concentrations in lamellipodia of moving cells. PLoS ONE 4, e4810.
42. Kovar, DR, Harris, ES, Mahaffy, R, Higgs, HN, and Pollard, TD (2006). Control of the assembly of ATP- and ADP-actin by formins and profilin. Cell 124, 423–435.
43. Kremers, G-J, Hazelwood, KL, Murphy, CS, Davidson, MW, and Piston, DW (2009). Photoconversion in orange and red fluorescent proteins. Nat Methods 6, 355–358.
44. Krishnan, K, and Moens, PDJ (2009). Structure and functions of profilins. Biophys Rev 1, 71–81.
45. Lambrechts, A, Jonckheere, V, Dewitte, D, Vandekerckhove, J, and Ampe, C (2002). Mutational analysis of human profilin I reveals a second PI(4,5)-P2 binding site neighbouring the poly(L-proline) binding site. BMC Biochem 3, 12.
46. Lassing, I, and Lindberg, U (1985). Specific interaction between phosphatidylinositol 4,5-bisphosphate and profilactin. Nature 314, 472–474.
47. Mammoto, A, Sasaki, T, Asakura, T, Hotta, I, Imamura, H, Takahashi, K, Matsuura, Y, Shirao, T, and Takai, Y (1998). Interactions of drebrin and gephyrin with profilin. Biochem Biophys Res Commun 243, 86–89.
48. Martys, JL, Wjasow, C, Gangi, DM, Kielian, MC, McGraw, TE, and Backer, JM (1996). Wortmannin-sensitive trafficking pathways in Chinese hamster ovary cells. Differential effects on endocytosis and lysosomal sorting. J Biol Chem 271, 10953–10962.
49. Michell, RH, Heath, VL, Lemmon, MA, and Dove, SK (2006). Phosphatidylinositol 3,5-bisphosphate: metabolism and cellular functions. Trends Biochem Sci 31, 52–63.
50. Miki, H, Suetsugu, S, and Takenawa, T (1998). WAVE, a novel WASP-family protein involved in actin reorganization induced by Rac. EMBO J 17, 6932–6941.
51. Moens, PDJ, and Coumans, JVF (2015). Profilin-1 mediated cell-cycle arrest: searching for drug targets. Cell Cycle 14, 3669–3670.
52. Nejedlá, M, Klebanovych, A, Sulimenko, V, Sulimenko, T, Dráberová, E, Dráber, P, and Karlsson, R (2021). The actin regulator profilin 1 is functionally associated with the mammalian centrosome. Life Sci Alliance 4, e202000655.
53. Nejedla, M, Li, Z, Masser, AE, Biancospino, M, Spiess, M, Mackowiak, SD, Friedländer, MR, and Karlsson, R (2017). A fluorophore fusion construct of human profilin I with non-compromised poly(L-proline) binding capacity suitable for Imaging. J Mol Biol 429, 964–976.
54. Nejedla, M, Sadi, S, Sulimenko, V, de Almeida, FN, Blom, H, Draber, P, Aspenström, P, and Karlsson, R (2016). Profilin connects actin assembly with microtubule dynamics. Mol Biol Cell 27, 2381–2393.
55. Niggli, V (2005). Regulation of protein activities by phosphoinositide phosphates. Annu Rev Cell Dev Biol 21, 57–79.
56. Nishimura, Y, Shi, S, Zhang, F, Liu, R, Takagi, Y, Bershadsky, AD, Viasnoff, V, and Sellers, JR (2021). The formin inhibitor SMIFH2 inhibits members of the myosin superfamily. J Cell Sci 134, jcs253708.
57. Pernier, J, Shekhar, S, Jegou, A, Guichard, B, and Carlier, M-F (2016). Profilin interaction with actin filament barbed end controls dynamic instability, capping, branching, and motility. Dev Cell 36, 201–214.
58. Pimm, ML, and Henty-Ridilla, JL (2021). New twists in actin-microtubule interactions. Mol Biol Cell 32, 211–217.
59. Pimm, ML, Hotaling, J, and Henty-Ridilla, JL (2020). Profilin choreographs actin and microtubules in cells and cancer. Int Rev Cell Mol Biol. 355, 155-204.
60. Pinto-Costa, R, and Sousa, MM (2019). Profilin as a dual regulator of actin and microtubule dynamics. Cytoskeleton 3-4, 76-83.
61. Pollard, TD, Blanchoin, L, and Mullins, RD (2000). Molecular mechanisms controlling actin filament dynamics in nonmuscle cells. Annu Rev Biophys Biomol Struct 29, 545–576.
62. Popov, AV, Severin, F, and Karsenti, E (2002). XMAP215 is required for the microtubule-nucleating activity of centrosomes. Curr Biol 12, 1326–1330.
63. Reinhard, M, Giehl, K, Abel, K, Haffner, C, Jarchau, T, Hoppe, V, Jockusch, BM, and Walter, U (1995).

The proline-rich focal adhesion and microfilament protein VASP is a ligand for profilins. EMBO J 14, 1583–1589.
64. Rodal, AA, Manning, AL, Goode, BL, and Drubin, DG (2003). Negative regulation of yeast WASp by two SH3 domain-containing proteins. Curr Biol 13, 1000–1008.
65. Rotty, JD, Wu, C, Haynes, EM, Suarez, C, Winkelman, JD, Johnson, HE, Haugh, JM, Kovar, DR, and Bear, JE (2015). Profilin-1 serves as a gatekeeper for actin assembly by Arp2/3-dependent and -independent pathways. Dev Cell 32, 54–67.
66. Schindelin, J et al. (2012). Fiji: an open-source platform for biological-image analysis. Nat Methods 9, 676–682.
67. Schutt, CE, Myslik, JC, Rozycki, MD, Goonesekere, NCW, and Lindberg, U (1993). The structure of crystalline profilin-beta-actin. Nature 365, 810–816.
68. Skare, P, and Karlsson, R (2002). Evidence for two interaction regions for phosphatidylinositol(4,5)-bisphosphate on mammalian profilin I. FEBS Lett 522, 119–124.
69. Skruber, K, Read, T-A, and Vitriol, EA (2018). Reconsidering an active role for G-actin in cytoskeletal regulation. J Cell Sci 131, jcs203760.
70. Skruber, K, Warp, PV, Shklyarov, R, Thomas, JD, Swanson, MS, Henty-Ridilla, JL, Read, T-A, and Vitriol, EA (2020). Arp2/3 and mena/VASP require profilin 1 for actin network assembly at the leading dge. Curr Biol 30, 2651-2664.e5.
71. Smith, BA, Padrick, SB, Doolittle, LK, Daugherty-Clarke, K, Corrêa, IR, Xu, M-Q, Goode, BL, Rosen, MK, and Gelles, J (2013). Three-color single molecule imaging shows WASP detachment from Arp2/3 complex triggers actin filament branch formation. Elife 2, e01008.
72. Spudich, JA, and Watt, S (1971). The regulation of rabbit skeletal muscle contraction. I. Biochemical studies of the interaction of the tropomyosin-troponin complex with actin and the proteolytic fragments of myosin. J Biol Chem 246, 4866–4871.
73. Suarez, C, Carroll, RT, Burke, TA, Christensen, JR, Bestul, AJ, Sees, JA, James, ML, Sirotkin, V, and Kovar, DR (2015). Profilin regulates F-actin network homeostasis by favoring formin over Arp2/3 complex. Dev Cell 32, 43–53.
74. Suarez, C, and Kovar, DR (2016). Internetwork competition for monomers governs actin cytoskeleton organization. Nat Rev Mol Cell Biol 12, 799–810.
75. Suetsugu, S, Miki, H, and Takenawa, T (1998). The essential role of profilin in the assembly of actin for microspike formation. EMBO J 17, 6516–6526.
76. Sun, T, Li, S, and Ren, H (2013). Profilin as a regulator of the membrane-actin cytoskeleton interface in plant cells. Front Plant Sci 4, 512.
77. Tarachandani, A, and Wang, YL (1996). Site-directed mutagenesis enabled preparation of a functional fluorescent analog of profilin: biochemical characterization and localization in living cells. Cell Motil Cytoskeleton 34, 313–323.
78. Vidali, L, and Hepler, PK (1997). Characterization and localization of profilin in pollen grains and tubes of Lilium longiflorum. Cell Motil Cytoskeleton 36, 323–338.
79. Vinson, VK, De La Cruz, EM, Higgs, HN, and Pollard, TD (1998). Interactions of Acanthamoeba profilin with actin and nucleotides bound to actin. Biochemistry 37, 10871–10880.
80. Wen, K-K, McKane, M, Houtman, JCD, and Rubenstein, PA (2008). Control of the ability of profilin to bind and facilitate nucleotide exchange from G-actin. J Biol Chem 283, 9444–9453.
81. Witke, W, Podtelejnikov, AV, Di Nardo, A, Sutherland, JD, Gurniak, CB, Dotti, C, and Mann, M (1998). In mouse brain profilin I and profilin II associate with regulators of the endocytic pathway and actin assembly. EMBO J 17, 967–976.
82. Witke, W, Sutherland, JD, Sharpe, A, Arai, M, and Kwiatkowski, DJ (2001). Profilin I is essential for cell survival and cell division in early mouse development. Proc Natl Acad Sci USA 98, 3832–3836.
83. Wittenmayer, N, Rothkegel, M, Jockusch, BM, and Schlüter, K (2000). Functional characterization of green fluorescent protein-profilin fusion proteins: GFP-profilin fusion proteins. Eur J Biochem 267, 5247–5256.
84. Xue, B, Leyrat, C, Grimes, JM, and Robinson, RC (2014). Structural basis of thymosin-β4/profilin exchange leading to actin filament polymerization. Proc Natl Acad Sci USA 111, E4596-4605.
85. Zweifel, ME, and Courtemanche, N (2020). Competition for delivery of profilin-actin to barbed ends limits the rate of formin-mediated actin filament elongation. J Biol Chem. 295, 4513-4525.

Supplemental Figure Legends

Figure S1. Full-blots associated with tagged profilin binding phosphoinositide (PIP)-lipids. **(A)** Western blot of supernatants and pellets from liposome pelleting assays containing 1 μM profilin in absence (control) or presence of 0.33 mM of either phosphatidylinositol 3,5-bisphoshate ($PI(3,5)P_2$) or phosphatidylinositol 4,5-bisphoshate ($PI(4,5)P_2$) lipids. **(B)** Western blot of supernatants and pellets from liposome pelleting assays containing 1 μM mApple-profilin in absence (control) or presence of 0.33 mM of $PI(3,5)P_2$ or $PI(4,5)P_2$. Profilin-1 B 10 was used as a primary antibody (1:5,000 dilution; SantaCruz 137235) and goat anti-mouse 926-32210 was used as the secondary antibody (1:10,000 dilution; LI-COR Biosciences).

Figure S2. Untagged profilin is unsuitable for conventional anisotropy assays. Fluorescence anisotropy measurement of 10 nM OG-actin mixed with increasing concentrations of unlabeled profilin. Unlabeled profilin is insufficient to elicit a change in anisotropy in our system (n = 1).

Figure S3. Localization of mApple-profilin with actin filaments in vitro. **(A)** Images from a multicolor TIRF movie of 1 μM actin monomers (10% Alexa-647-labeled; 0.6 nM biotin-actin) (cyan) polymerizing in the presence of 3 μM mApple-profilin-1 (pink). Tagged-profilin suppresses actin filament polymerization and rarely associates with actin filaments (one example is shown in the white box). Scale bar, 20 μm. **(B)** Zoomed in view of box in (A) showing the single observed example of mApple-profilin localized to the growing end of an actin filament. Scale bar, 10 μm. **(C)** Quantification of mApple-profilin association with actin filaments. All actin filaments from movies obtained (n = 3) were assessed for colocalization between mApple-profilin molecules with any portion of actin filaments from TIRF reactions as (A).

Figure S4. Full views of the effects of mApple-profilin on formin-mediated actin assembly. **(A)** Full views of montages of formin-mediated actin polymerization. Reactions contain 1 μM actin (10% Alexa-647-labeled; 0.6 nM biotin-actin) and 25 nM mDia1(FH1-C) and 5 μM profilin or 5 μM mApple-profilin. White box indicates the view presented in Figure 4B. Only the actin-wavelength (647 nm) is shown. **(B)** Full view of a multi-color time lapse TIRF montage. Reaction contains 1 μM actin (10% Alexa-647-labeled; 0.6 nM biotin-actin), 25 nM mDia1(FH1-C) and 5 μM mApple-profilin. The actin (647 nm) and mApple (561 nm) wavelengths are shown individually and merged. Scale bars, 20 μm.

Figure S5. Additional views of the effects of tagged profilin on microtubule dynamics. **(A)** Full views of montages displaying the effects of profilin on microtubule dynamics. Reactions contain 647-biotinylated-GMP-CCP microtubule seeds (not shown), 10 μM free tubulin (5% HiLyte488) and 5 μM profilin-1 (unlabeled) or 5 μM mApple-profilin-1. Black box indicates the view presented in Figure 5A. **(B)** Full view of a multi-color time lapse TIRF montage. Reaction contains 10 μM free tubulin (5% HiLyte488) and 5 μM mApple-profilin-1. Black box indicates the view presented in Figure 5H. Scale bars, 20 μm. **(C)** Montage of a single-microtubule from reactions as in (Figure 5H) showing each wavelength (and merge) of the view presented in Figure 5J. + and - indicate the microtubule polarity. Scale bar, 10 μm.

Figure S6. Full-blots used to determine profilin levels in Neuroblastoma-2a (N2a) cells. Full blots confirming CRISPR knockout and rescue of profilin-1 with either mAp-PFN1 or Halo-PFN1 constructs. N2a cell extracts were prepared from wild-type N2a ($PFN^{+/+}$), profilin knockout ($PFN1^{-/-}$), or profilin knockout cells 24 h after transfection with a tag-less rescue construct, mAp-PFN1, or Halo-PFN1. **(A)** Blots were probed with Profilin-1 B 10 primary (1:3,500 dilution; SantaCruz 137235) and goat anti-mouse 926-32210 secondary (1:5,000 dilution; LiCor Biosciences) antibodies and also **(B)** α-tubulin primary (1:10,000; Abcam 18251) and donkey anti-rabbit secondary (1:20,000; 926-68073). **(C)** Coomassie stained membrane from (A) is shown as a loading control. **(D)** View of a full representative blot that was used to determine the concentration of endogenous profilin-1 in N2a cells. Blot was probed as in (A) for profilin-1 (D) or α-tubulin **(E)** and later **(F)** Coomassie stained to compare to known quantities of purified mApple-profilin (43 kDa) or untagged profilin (15 kDa).

Supplemental Movie 1. TIRF microscopy comparing the effects of unlabeled profilin-1 or mApple-profilin-1 on actin assembly. Reaction components: 1 μM actin monomers (20% Oregon Green (OG)-labeled; 0.6 nM biotin-actin). Variable components 3 μM profilin-1 (unlabeled) or 3 μM mApple-profilin-1. Only the actin wavelength (488 nm) is shown. Video playback is 10 frames per s. Scale bars, 10 μm.

Supplemental Movie 2. Multi-color TIRF microscopy of mApple-profilin on actin assembly. Reaction components: 1 μM actin monomers (20% OG-labeled; 0.6 nM biotin-actin) (cyan) and 3 μM mApple-profilin-1 (pink). The actin (488 nm) and mApple (561 nm) wavelengths are shown individually and merged. White box corresponds to montage inset from Figure S3B. Video playback is 10 frames per s. Scale bars, 10 μm.

Supplemental Movie 3. TIRF microscopy comparing the effects of unlabeled profilin-1 or mApple-profilin-1 on formin-mediated actin filament assembly. Reaction components: 1 μM actin monomers (10% Alexa-647-labeled; 0.6 nM biotin-actin). Variable components 5 μM profilin-1 (unlabeled) or 5 μM mApple-profilin-1. Only the actin wavelength (647

nm) is shown. White box corresponds to montage from Figures 4B and S4A. Video playback is 10 frames per s. Scale bars, 10 µm.

Supplemental Movie 4. Multi-color TIRF microscopy of mApple-profilin on formin-mediated actin filament assembly. Reaction components: 1 µM actin monomers (10% Alexa-647-labeled; 0.6 nM biotin-actin) (cyan) and 5 µM mApple-profilin-1 (pink). The actin (647 nm) and mApple (561 nm) wavelengths are shown individually and merged. Video playback is 10 frames per s. Scale bars, 10 µm.

Supplemental Movie 5. TIRF microscopy comparing the effects of unlabeled profilin-1 or mApple-profilin-1 on microtubule dynamics. Reaction components: 647-biotinylated-GMP-CCP microtubule seeds (not shown), 10 µM free tubulin (5% HiLyte488). Variable components 5 µM profilin-1 (unlabeled) or 5 µM mApple-profilin-1. Only the polymerizing microtubule wavelength (488 nm) is shown. Black box corresponds to montage inset from Figure 5A Video playback is 10 frames per s. Scale bars, 20 µm.

Supplemental Movie 6. Multi-color TIRF microscopy of mApple-profilin on microtubule dynamics. Reaction components: 647-biotinylated-GMP-CCP microtubule seeds (not shown), 10 µM free tubulin (5% HiLyte488) (black) and 5 µM mApple-profilin-1 (pink). The polymerizing microtubule (488 nm) and mApple-profilin wavelengths (561 nm) are shown individually and merged. Box corresponds to montage inset from Figure 5H. Video playback is 10 frames per s. Scale bars, 20 µm.

Supplemental Movie 7. Profilin transiently binds and diffuses along the microtubule lattice. Reaction components: 647-biotinylated-GMP-CCP microtubule seeds (not shown), 10 µM free tubulin (5%HiLyte488) (black) and 5 µM mApple-profilin-1 (pink). The polymerizing microtubule (488 nm) and mApple-profilin wavelengths (561 nm) are shown individually and merged. + and - indicate the microtubule polarity. Video playback is 10 frames per s. Scale bar, 10 µm.